Article:

Paul, F, Bolch, T, Kääb, A et al. (22 more authors) (2015) The glaciers climate change initiative: Methods for creating glacier area, elevation change and velocity products. Remote Sensing of Environment, 162. pp. 408-426. ISSN 0034-4257

https://doi.org/10.1016/j.rse.2013.07.043

The Glaciers Climate Change Initiative: Methods for creating glacier area, elevation change and velocity products

Frank Paul[1], Tobias Bolch[1], Andreas Kääb[2], Thomas Nagler[3], Christopher Nuth[2], Killian Scharrer[3], Andrew Shepherd[4], Tazio Strozzi[5], Francesca Ticconi[4], Rakesh Bhambri[6], Etienne Berthier[7], Suzanne Bevan[8], Noel Gourmelen[9], Torborg Heid[2], Seongsu Jeong[10], Matthias Kunz[11], Tom Rune Lauknes[12], Adrian Luckman[13], John Peter Merryman Boncori[14], Geir Moholdt[15], Alan Muir[16], Julia Neelmeijer[17], Melanie Rankl[18], Jeffrey VanLooy[19], Thomas Van Niel[20]

1 Department of Geography, University of Zurich, Switzerland
2 Department of Geosciences, University of Oslo, Norway
3 Environmental Earth Observation IT GmbH (ENVEO), Innsbruck, Austria
4 School of Earth and Environment, University of Leeds, UK
5 Gamma Remote Sensing AG, Gümligen, Switzerland
6 Centre for Glaciology, Wadia Institute of Himalayan Geology, 33 GMS Road, Dehradun - 248001, India
7 CNRS, Universitè de Toulouse, LEGOS, 14 avenue Ed. Belin, Toulouse 31400, France
8 Swansea University, Swansea, UK
9 Institut de Physique du Globe de Strasbourg, University Strasbourg, France
10 Ohio State University, Columbus, OH, USA
11 School of Civil Engineering and Geosciences, Newcastle University, NE1 7RU, UK
12 Norut, P.O. Box 6434, NO-9294 Tromsø, Norway
13 Swansea University, Swansea, SA2 8PP, Wales, UK
14 Istituto Nazionaledi Geofisicae Vulcanologia, Rome, Italy
15 Scripps Institution of Oceanography, La Jolla, CA, USA
16 Centre for Polar Observation and Modelling, United Kingdom
17 Helmholtz Centre Potsdam, GFZ German Research Centre for Geosciences, Potsdam, Germany
18 University of Erlangen, Erlangen, Germany
19 Department of Earth System Science and Policy, University of North Dakota, Grand Forks, ND, 58202, USA
20 CSIRO Land and Water, Private Bag No. 5, Wembley, WA 6913, Australia

Abstract

Glaciers and their changes through time are increasingly obtained from a wide range of satellite sensors. Due to the often remote location of glaciers in inaccessible and high-mountain terrain, satellite observations frequently provide the only available measurements. Furthermore, satellite data provide observations of glacier characteristics that are difficult to monitor using ground-based measurements, thus complementing the latter. In the Glaciers_cci project of the European Space Agency (ESA), three of these characteristics are investigated in detail: glacier area, elevation change and surface velocity. We use (a) data from optical sensors to derive glacier outlines, (b) digital elevation models from at least two points in time and (c) repeat altimetry for determining elevation changes, and (d) data from repeat optical and microwave sensors for calculating surface velocity. For the latter, the two sensor types provide complementary information in terms of spatio-temporal coverage. While (c) and (d) can be generated mostly automatically, (a) and (b) require the intervention of an analyst. Largely based on the results of various round robin experiments (multi-analyst benchmark studies) for each of the products, we suggest and describe the most suitable algorithms for product creation and provide recommendations concerning their practical implementation and the required post-processing. For some of the products (area, velocity) post-processing can influence product quality more than the main-processing algorithm.

1. Introduction

Glaciers are considered key indicators of climate change due to their sensitive reaction to even small climatic changes (e.g. Lemke et al., 2007). This is mainly a result of the ice being at pressure melting point (under terrestrial conditions and for temperate glaciers), i.e. any surplus energy melts the ice. Glaciers adjust their geometry (extent and surface elevation) to equilibrate with the prevailing climatic conditions that largely control mass gain and loss. Thereby, glacier flow transports the mass gained in the accumulation to the ablation region where it melts. The determination of changes in glacier geometry that occur as a reaction to climate change thus involves the measurement of change in glacier surface elevation, flow velocity and size/length, among others (e.g. snow covered area at the end of the melting period). Variations in these parameters are related to each other at varying time scales. For example, the annual mass budget is a direct reaction to the prevailing meteorological conditions over a year, whereas changes in flow velocity result from a more long-term change in the nourishment of a glacier (Span and Kuhn, 2003). Also changes in glacier length and size follow more long-term climatic changes, so that a direct cause and effect relation is difficult to resolve (e.g. Johannesson et al., 1989).

Due to the often remote location and wide areal extent of glaciers, satellite-based measurements of glacier changes complement field-based surveys. Satellite data can largely extend the number of glaciers measured, the time period covered and the parameters that can be assessed. The wide range of available sensors (e.g. imaging sensors and altimeters working in both the optical and microwave region of the electromagnetic spectrum) and archives from ongoing and historic missions combined with already existing geospatial information like digital elevation models (DEMs) or former glacier outlines as available from GLIMS (Global Land Ice Measurements from Space), allows measurement of a wide range of glaciologically relevant parameters (Kargel et al., 2005; Malenovsky et al., 2012; IGOS, 2007). The Glaciers_cci project focuses on three of these parameters: glacier area, elevation changes (from DEM differencing and repeat altimetry), and surface velocity fields (from optical and microwave sensors). Numerous algorithms are available for product retrieval from each of the input data sets and sensor combinations. They differ in complexity (from simple arithmetics such as division or subtraction of raw data to rather complex calculations and processing lines) and in the required operator interaction (e.g. from manual control and editing to almost fully automatic processing), but a pre-, main- and post-processing stage is common to all of them. In general, only the main processing stage is automated while the other stages require operator interaction. The consistency of the manual corrections applied in the post-processing stage are critical when products are derived in a globally collaborative effort such as for GLIMS (Kargel et al., 2005; Raup et al., 2007).

Accordingly, a major objective of the Glaciers_cci project is to find the most suitable algorithms for data processing and an improved error characterisation of the generated products. For this purpose we performed an analysis of various existing algorithms along with their specific post-processing and editing operations in four round robin experiments (one for glacier area and surface velocity, and two for elevation change). In each of the following product-related sections we provide a short overview of the algorithms applied based on earlier studies and either summarise (if already published) or illustrate in detail the set-up and results of the round robin experiments for each product. We also describe the challenges and main pitfalls that might occur during the pre- and post-processing stages by operators, as this always involves some subjectivity and has an impact on the quality of the final product. The study regions for the product-specific round robin experiments are located in different mountain ranges around the world (Fig. 1). These regions were selected for a range of criteria such as availability of validation data or satellite data from different sensors, typical challenges, clear identification of the target, and glacier size.

Figure 1

2. Glacier area

2.1 Background and previous work

Satellite data have been used to study glaciers from the very beginning of their availability. Starting with the mapping of different ice and snow facies using the ca. 80 m resolution Landsat Multi Spectral Scanner (MSS) sensor in the 1970s (Østrem, 1975; Rott, 1976) and the 30 m Landsat Thematic Mapper (TM) sensor a decade later (e.g. Hall et al., 1987; Williams et al., 1991), the 1990s saw mapping of glacier extent and first studies on change assessment with TM data (e.g. Bayr et al., 1994, Aniya et al., 1996, Jacobs et al. 1997). A wide range of methods were applied in these and other studies to map glacier extents. They range from full manual on-screen digitisation (e.g. Rott and Markl, 1989; Williams et al., 1997), to the segmentation of ratio images (e.g. Bayr et al., 1994; Rott, 1994; Paul, 2002) and various supervised (Maximum-Likelihood) and unsupervised (ISODATA clustering) algorithms (e.g. Aniya et al., 1996; Sidjak and Wheate, 1999). All methods utilise the very low spectral reflectance of ice and snow in the shortwave infrared (SWIR) versus the high reflectance in the visible spectrum (VIS) to identify glaciers (e.g. Dozier, 1989).

Severeal methods have been compared in regard to their performance (e.g. computation time, accuracy) in a relative sense (e.g. Albert, 2002; Paul and Kääb, 2005), as well as against higher-resolution datasets (serving as a reference) to determine their absolute accuracy (e.g. Andreassen et al., 2008; Paul et al., 2003). However, this is a challenging task as also high-resolution data might not provide a reference with higher accuracy (Paul et al., 2013). In the last decade, remote sensing data have been used more systematically to create glacier inventories in many regions of the world (e.g. Bolch et al. 2010; Frey et al., 2012; Le Bris et al., 2011; Khromova et al., 2006; Kulkarni et al., 2007; Paul et al., 2011; Racoviteanu et al., 2008; Shangguan et al., 2009) with the majority of the studies using Landsat data. Several of them were made possible by the opening of the Landsat archive at USGS and the provision of all scenes as orthorectified images (Level 1T product) in Geotif format (Wulder et al., 2012).

Converting the glacier outlines to inventory information involves digital intersection with drainage divides and calculation of topographic parameters (e.g. minimum, mean, and maximum elevation) for each glacier entity. Practical guidelines (e.g. Raup and Khalsa, 2007; Racoviteanu et al., 2009) and general advice (e.g. Paul et al., 2002 and 2009) have been prepared for the analysts contributing to GLIMS allowing a more consistent data processing. The generated outlines are stored as shapefiles (a vector format) along with their meta-information in the GLIMS glacier database (www.glims.org) for free access by the community (Raup et al., 2007). One globally complete dataset of glacier outlines has recently been made available as the Randolph Glacier Inventory (RGI) via the GLIMS website (Arendt et al., 2012).

2.2 Pre-processing

For the glacier area product we here describe the lessons learned from previous studies, as a large part of the results of the round robin (accuracy assessment) were already published (Paul et al., 2013). The results of the algorithm selection resulting from the round robin are described in section 2.5. The first step in creating accurate glacier outlines from satellite data is the selection of suitable images. This is a non-trivial task, as snow and cloud conditions are often not optimal (e.g. clouds covering parts of an otherwise perfect scene) and it might be required to digitally combine several scenes of the same region (e.g. Bolch et al., 2010; Le Bris et al., 2011; Frey et al., 2012; Rastner et al., 2012; Bajracharya and Mool, 2011). Experience from the past decade has shown that it is not advisable to use scenes with adverse snow conditions (i.e. with seasonal snow outside of glaciers) for glacier mapping. The workload to correct these regions after an automated mapping of clean ice can be huge as a decision on thousands of small polygons has to be made. A size-filter is an option to remove many of the smallest snow patches, but if they are as large as glaciers (e.g. >0.05 km^2), manual editing might have to be applied. As the workload can be very high for this editing and the quality of the result still unsatisfactory, it is recommended to use only the best available scenes (in regard to snow conditions) for glacier mapping (e.g. Racoviteanu et al., 2009). The availability of full resolution preview images from the glovis.usgs.gov website for

Landsat data allows a fast analysis of the snow and cloud conditions, facilitating the selection of suitable images before downloading and processing the original data.

Once scenes are selected, they have to be downloaded, converted to the format of the digital image processing software used, and analysed in more detail. For this purpose and for any subsequent manual editing, it is recommend to generate contrast enhanced false-colour composites using the TM equivalent bands 3, 2, 1 (321), 432 and 543 as RGB (red, green, blue), respectively. The latter is important for proper identification of glaciers (appearing blue-green) and clouds (white), while the first helps to identify ice and snow in shadow during visual inspection. The typical false colour infrared image (bands 432) is useful for the identification of water surfaces that show a wide range of colours in this band combination. As the main processing works on the raw digital numbers, the otherwise often required atmospheric and/or topographic correction of the scenes need not be applied.

2.3 Main processing: Classification of glaciers

Glacier ice originates from metamorphosed and compressed snow resulting in spectral characteristics that are similar to those of snow with large grain size (Hall et al., 1987). At the end of the ablation period (when snow cover is minimal) and from a remote sensing perspective, the glacier surface is composed of bare ice, snow, dirt / debris / rocks and liquid water; all under highly variable illumination conditions (e.g. located in direct sunlight or cast shadow). Heavily crevassed regions can also lack spectral contrast (due to shadow) and debris-covered glacier parts are spectrally similar to the surrounding terrain and are thus not mapped as a part of a glacier. On the other hand, dirt often covers the bare ice on a micro scale, providing a sufficiently large portion of ice being visible when seen at a 30 m resolution and thus allowing its identification.

From the numerous methods applied previously for glacier classification (see section 2.1) the simple band ratio method emerged as a 'best' (i.e. most suitable) one (e.g. Albert 2002; Paul et al., 2002; Paul and Kääb, 2005). Compared to all others, the method is more fast, simple, accurate and robust (e.g. results are rather insensitive to the selected threshold). The method is based on the application of a threshold to a simple band ratio with the equivalent bands of TM3 (red) and TM5 (SWIR) and an additional threshold in TM1 (for improved mapping in shadow) using raw digital numbers. When TM4/TM5 is applied instead, the TM1 threshold is not required as TM4 is less sensitive to atmospheric scattering than TM3 and rocks in shadow are not mapped as glaciers. The TM3/TM5 ratio also tends to map most water surfaces as glaciers (depending on turbidity), which is less the case with TM4/TM5. On the other hand, TM4/TM5 tends to miss regions with ice and snow in deep cast shadow (e.g. Andreassen et al., 2008), but might map vegetation in shadow as glaciers. Hence, preference for one or the other band combination depends on the water / vegetation conditions in the respective regions. Also the normalised difference snow index (NDSI) computed as (TM2-TM5)/(TM2+TM5) is applied widely for glacier mapping (e.g. Racoviteanu et al., 2008; Gjermundsson et al., 2011), but it requires more user interaction as the atmospheric scattering in TM2 (green) is high and the path radiance has to be subtracted beforehand (Paul and Kääb, 2005). This requires calculation of a histogram, determination of its lowest suitable value, and subtraction of this value from the original band before the NDSI can be applied.

The selected threshold is converting the ratio image (floating point) to a binary (black and white only) glacier map. The threshold for TM1 is only applied to regions that have been classified as glaciers in the step before. Typical values of the threshold published in the above cited literature are in the 2.0 ±0.5 range for the ratio and 60 ±30 for the TM1 correction, partly depending on the band combination used and the local atmospheric conditions. The method works for sensors like ASTER and SPOT as well, but different threshold values might apply, as only a green band (equivalent to TM2) is available and gain settings of individual bands can differ (Kääb et al., 2003). As shown in Fig. 2a, the threshold for the ratio is rather robust, i.e. only a few pixels change when 1.8, 1.9 or 2.0 is used as a threshold (cf. Paul and Hendriks, 2010). However, the TM1 threshold is more sensitive and small changes in the threshold value (e.g. +/-10) can result in large difference in the mapped glacier region (Fig. 3). The general advice for threshold selection is thus to check this in a region of shadow using a value that minimises the workload for post-processing (i.e. manual corrections required in shadow regions). The values are found by first selecting the threshold for the band ratio and then optimising the TM1 value (green band for ASTER and SPOT). When comparing glacier outlines from different thresholds, the optimal value is where most ice is mapped (i.e. towards low threshold values), but noise is still low. As can be seen in Fig. 3, more ice and snow in shadow is mapped towards the lower thresholds in TM1, but the lowest value (60) starts to introduce noise (small yellow dots). In this case 65 was finally selected as a threshold value for TM1. After the binary image is created, a spatial filter (e.g. 3 by 3 median) may be applied without changing the glacier area much (cf. Paul and Hendriks, 2010), i.e. the number of removed and added pixels is about similar as can be seen in Fig. 2b. In this regard it is acceptable to have some noisy pixels left in the previous step, as they will be removed by the filter. Once the final glacier map is created, a raster-vector conversion is applied for the subsequent editing of polygons in the vector domain.

Figure 2

Concerning a potential automated detection of the correct threshold, it remains to be tested whether the use of at-satellite planetary reflectance (correcting for solar elevation and Sun-Earth distance) would result in more unique threshold values globally. As shown previously, locally variable atmospheric conditions (e.g. due to fog, haze or optically thin clouds) might require the use of different thresholds within one scene or even require to map the upper and lower parts of glaciers from different scenes (e.g. Bolch et al., 2010; Le Bris et al., 2011; Rastner et al., 2012) and digitally combine both datasets afterwards.

Figure 3

2.4 Post-processing (Manual editing)

Post-processing can be divided into three steps, (i) manual correction of glacier outlines, (ii) digital intersection with drainage divides, and (iii) calculation of topographic parameters for each glacier from the DEM (e.g. mean, maximum and minimum elevation). The focus is in the following on (i), as (ii) and (iii) were already described in detail by Paul et al. (2002) and Paul et al. (2009), respectively. The generation of drainage divides from watershed analysis is required for (ii) and, among others, already described by Bolch et al. (2010), Manley (2008) or Schiefer et al. (2008).

A first step for (i) is to remove all gross errors (e.g. isolated lakes and rivers), as misclassified water surfaces not in contact with glacier ice or those with ice bergs or sea ice on it tend to create (ten-)thousands of polygons that reduce processing speed during editing. These polygons can easily be selected in the vector domain and deleted. The next step is the more detailed correction of debris-covered parts, shadow regions, local clouds hiding a glacier's perimeter and terminus digitizing of glaciers calving into lakes or the sea. In this step the various false-colour composites created during pre-processing are used in the background for correcting the outlines, but simple overlay of the three individual bands (layer-stacking) might also work for proper correction. High-resolution images as sometimes available in Google Maps^{TM} or similar tools, can be used to aid in the correct interpretation of glacier outlines. In cases where the exact boundary is unclear (e.g. due to deep shadow or clouds), we suggest using this additional information and, if a DEM is available, to also create a shaded relief and manually digitize the outline as a best-guess interpretation.

2.5 The glacier area round robin

Most of the methods applied previously for glacier mapping (e.g. band ratio, NDSI, ISODATA clustering, principal component analysis and decision tree classifiers) were also applied by the participants of the round robin to a challenging test site in the western Himalaya (with many debris-covered glaciers). For a subregion of the full scene the participants were asked to create glacier outlines from their algorithm of choice and correct the wrongly classified outlines manually using only spectral information for identification (i.e. a DEM was not provided). A digital overlay of all resulting glacier outlines is shown in Fig. 4, revealing differences only at the level of individual pixels (i.e. most outlines are on top of each other) for the automated mapping and independent of the method applied. On the other hand, large differences are visible in debris-covered regions where manual corrections were applied. This result confirms earlier studies that mentioned debris-cover being a major error source (e.g. Paul et al, 2013; Racovitenau et al., 2008; Shukla et al., 2011). The applied manual corrections are rather consistent where the debris cover is easy to distinguish (e.g. through a different colour or shading) and deviations increase as the interpretation becomes more difficult (e.g. the isolated orange lines in Fig. 4). The change in glacier size due to the added debris cover can be 50% or more of the original size. This is about one order of magnitude higher than the accuracy of the clean ice mapping (e.g. Paul et al., 2013), and thus a crucial factor when deriving glacier area changes. In other words, the round robin confirmed that the differences due to the algorithm used for the mapping are minor with respect to product quality when glaciers are debris covered.

Figure 4

3. Glacier elevation changes from DEM differencing

3.1 Background and previous works

Measuring changes in glacier elevation is a commonly applied method for estimating volume and mass changes of glaciers at local and regional scales. To avoid confusion, we use in this study elevation as defined by McVicar and Körner (2013). The geodetic method was applied for decades to DEMs derived from aerial photographs (Finsterwalder, 1954) and, in the last decade, to DEMs derived from space-borne data. For individual glaciers, geodetic mass balances over decadal periods are useful to check the consistency with cumulated *in-situ* measured mass balance and to determine whether bias has accumulated in the *in-situ* measurements (e.g. Cox and March, 2004; Soruco et al., 2009; Zemp et al., 2010). Importantly, the same method allows determination of region-wide mass balance due to the large spatial coverage of recent space-borne DEMs (e.g. Berthier et al., 2010; Bolch et al., 2011; Gardelle et al., 2012b; Larsen et al., 2007; Paul and Haeberli, 2008; Schiefer et al., 2007; Willis et al., 2012). Besides the spatial representativeness of elevation change measurements, the most critical and much discussed assumption required for converting elevation and volume changes into mass changes is the density of the material gained or lost (cf. Kääb et al., 2012; Huss, 2013). Elevation and volume change measurements are free of related hypotheses and can thus be independently converted to mass changes at a later point using a density scenario of choice.

DEMs may be generated through airborne or space-borne techniques using photogrammetry on optical images, interferometry on microwave images and LIDAR scanning. Each of these methods has different types of errors (in glacier settings) that must be considered independently. For example, photogrammetry applied to optical images is dependent upon good visual contrast, while radar interferometry is limited by coherence (signal de-correlation with time) and may also provide elevations of a layer below the glacier surface (radar wave penetration), and LIDAR have range biases or waveform saturation problems (Fricker et al., 2005; Joerg et. al., 2012). It is important to note that the impact of these and other general method characteristics will vary considerably depending on glacier type and setting, and on specific ground conditions during acquisition, so that DEM quality is highly variable in space, time and with the method employed. Table 1 provides an overview of automatically generated DEMs available for computing glacier elevation changes globally.

Table 1

Glaciers_cci focused specifically on the extraction of elevation changes, as the conversion to mass changes can be completed by the users with their preferred density assumption. Subtraction of two matrices (i.e. DEMs) is trivial when having the same ground resolution; however ensuring the proper alignment of the DEMs, that their resolutions are similar, and the detection of other higher-order biases remains difficult. It was previously shown that even sub-pixel horizontal misalignment between DEMs can cause large bias in elevation change estimates (Van Niel et al., 2008; Nuth and Kääb, 2011). This means that co-registration of DEMs is of primary concern when estimating elevation change through DEM differencing. Therefore, this round robin tested co-registration algorithms for determining mis-alignments between the multitemporal DEMs (the general procedures are outlined below). The slave DEM was defined as that which was co-registered to the master DEM.

3.2 Pre-processing

To compute elevation differences, the DEMs must be in the same map projection. Commonly, rectangular coordinate systems such as the Universal Transverse Mercator (UTM) system are used as this projection has limited distortions within individual UTM zones and re-projection algorithms are commonly available in GIS software. Multi-temporal DEMs may also have different spatial resolutions, which require resampling of one or both of the DEMs to make them congruent. Resampling should be performed using algorithms more advanced than nearest neighbor (i.e. bilinear, bi-cubic, etc.), as nearest neighbour might result in sub-pixel horizontal misalignments between the data. The simplest method to determine whether the two DEMs are co-registered is to map their differences in gray-scale or a dichromatic color ramp centered around 0 (Nuth and Kääb, 2011). If the grayscale differences resemble the terrain (looking like a DEM hillshade) then there is a horizontal misalignment. The bearing of the overall shift between DEMs is associated with the aspect having the highest positive bias, whereas the magnitude of the bias is associated with the slope of the site (Van Niel et al., 2008), as shown in Fig. 5. The relationship between elevation difference and both slope and aspect were formally defined in Nuth and Kääb (2011) and is summarised in Eq. (1).

Figure 5

3.3 The co-registration round robin

Test site, methods and results

The round robin for deriving glacier elevation changes from DEM differencing tested co-registration algorithms. The experiment covered the Southern Alps of New Zealand using two ASTER DEMs (2002 and 2006) and the SRTM DEM (2000), with optional auxiliary ICESat data. A common glacier mask (Gjermundsen et al., 2011) was provided together with the elevation datasets. Participants were asked to co-register the three DEMs to each other, and if possible, also to ICESat, return their co-registration parameters (Δx, Δy, Δz) and an elevation change grid (2006-2000). Six contributions implemented in various software products or combinations thereof (IDL, Matlab, ArcGIS, ENVI, PCI Geomatica, GMT tools, GDAL) were received. Three automatic algorithms were tested: (A) a robust surface matching technique solving for linear translation, rotation and scale (Gruen and Akca, 2005; Miller et al., 2009; Miller et al., 2008), (B) an iterative minimization of the elevation difference residuals (Berthier et al., 2007; Rodriguez et al., 2006), (C) an analytical solution for translation only based upon terrain slope and aspect (Kääb, 2005a; Nuth and Kääb, 2011) and (D) one semi-manual approach based upon terrain slope (VanLooy and Foster, 2008). The first algorithm minimises the sum of squares of the Euclidean distances between two surfaces while the other algorithms rely on the minimisation of elevation difference residuals over assumed stable terrain. The strategy for analyzing the results was to visualize the elevation change grids in grayscale to determine whether some misalignment remained ("false hillshade") and to compute the vector sum of three or more co-registration vectors between the datasets that should form a perfect triangle. Theoretically, the vector sums should be 0 for the horizontal and vertical components, but in practice residuals are present reflecting the method's uncertainty.

Table 2 shows the co-registration vectors and triangulation between the SRTM DEM (2000) and two ASTER DEMs (2002, 2006) for the three automatic algorithms tested (A, B and C described above). The specific co-registration parameters are similar for methods A and C (Table 2), but different for Method B when the SRTM DEM is involved. The reason behind this variation is that the SRTM DEM was provided with an additional world file (tfw) for geocoding, which does not specify the pixel definition of centre or corner. Nonetheless, the triangulation of co-registration parameters for all three algorithms resulted in similar sub-pixel residuals despite the variation in co-registration parameters. The "false-hillshade" of the DEM differences for 4 out of 6 contributions displayed only small hints of the terrain suggesting that the co-registration was successful and misalignment properly removed. In two cases, the terrain was clearly visible despite proper triangulation residuals. This occurred after co-registration in one software, and final differencing in another software, specifically from a nearest neighbour resampling that is default within the 'Raster Calculator Tool' of the ESRI ArcGIS software. In some of the contributions using the same algorithms (not shown here), the triangulated residuals resulted in magnitudes of similar order to the pixel and half pixel sizes of the DEMs. We attribute this artifact to the variable definition of the pixel corner vs. centre in the various software products, so it occurs specifically when switching software products within a single processing chain. In summary, one of the major lessons learned from this round robin was that any automated DEM differencing processing chain should be maintained within one software product to avoid propagation of pixel definition problems.

Table 2

Algorithm selection

All three automatic algorithms resulted in similar sub-pixel accuracies when co-registering DEMs. When co-registering a DEM to ICESat, the analytical solution using slope/aspect out-performed the other methods (Table 2). In terms of computational efficiency, the implementation of the analytical solution (C) requires 2-3 iterations whereas both the robust surface matching (A) and the image matching (B) required substantially more iterations. For development within Glaciers_cci, the analytical co-registration algorithm was therefore chosen due to its robustness to operate with various input datasets (i.e. the algorithm works equally well using either one DEM and one vector data set such as ICESat or between two DEMs) as well as algorithm efficiency. The algorithm is described in Nuth and Kääb (2011), and is based upon minimising the residuals between the left and right sides of equation (1) using the population of elevation differences on stable terrain (*dh*):

$$\frac{dh}{\tan(\alpha)} = a \cdot \cos(b - \psi) + c \qquad \text{(Eq. 1)}$$

where α is terrain slope, ψ is terrain aspect, and the parameters a and b are the magnitude and direction, respectively, of the co-registration vector and c is the mean bias between the DEMs divided by the mean slope of the selected terrain. The implementation for minimisation is not strictly defined, and we use a robust linear least squares method (implemented in Matlab) to determine unknown *a, b* and *c*. Since the solution to this analytical relationship is solved using a non-analytical surface (i.e. the terrain), the first solution may not be the final solution and iteration of the process is required to arrive at an ultimate solution. Typically 1-2 additional iterations are required (depending upon the minimisation routine); we stop the process when improvement of the standard deviation is less than 2%. An example of the co-registration procedure using the selected algorithm can be seen in Figure 5.

3.4 Main Processing

After determining the co-registration parameters, the original slave DEM was translated by adjusting the corner coordinates with the horizontal co-registration parameters (Δx, Δy) and the mean bias (Δz) being subtracted. Therefore, no resampling of the original pixels is required in this adjustment. Resampling of one of the DEMs was necessary to unify the two DEM pixel sizes and locations. In many cases (and in our round robin experiment), the coarser resolution DEM was over-sampled to the finer resolution DEM. However, this introduces data at a scale that is not measured by the technique, possibly introducing artifacts (Gardelle et al., 2012a; Paul, 2008). We suggest to under-sample the DEM with the finer resolution to that of the coarser resolution, preferably using block averaging filters if one DEM pixel size is at least two times larger than the other DEM pixel. After the DEMs cohere to each other in space and resolution, a matrix (map) of glacier elevation changes was generated by subtracting the two co-registered matrices (DEMs).

3.5 Post-processing

The co-registration procedure was the first-order correction required for the estimation of glacier elevation changes from DEM differencing, common to all DEM data sources. A number of other data source specific artifacts (biases) have been encountered in DEM differencing including C-Band penetration into snow-ice of the SRTM DEM (Berthier et al., 2006; Gardelle et al., 2012a; Kääb et al., 2012), along-track satellite attitude pointing biases in ASTER DEMs (Nuth and Kääb, 2011) and many other potential corrections such as sensor specific influences (e.g. Berthier et al., 2007; Paul, 2008; Bolch et al., 2008) and/or rotation/scale distortions may need to be considered. However, it remains unresolved what exactly could cause and what the physical meaning behind potential rotational/scale effects in differenced DEMs could be and whether their correction is required. Nonetheless, these effects have the potential to be incorporated in an automated DEM differencing processing chain if/when their corrections reach sufficient maturity for automated implementation. Alternatively, they may be bundled into one co-registration adjustment, such as that applied by Miller et al. (2008). This might also be important for DEM differencing with DEMs made from historical imagery (Kunz et al., 2012). Using the same co-registration method as proposed here, these higher order biases might require individual case-specific assessment.

The final post processing procedures included error estimation for the glacier elevation change measurements. We relied on statistical error modeling using estimates based upon the selected stable terrain assuming that the elevation measurement technique behaves similarly on and off glaciers, which in some cases (i.e. optical photogrammetry) may not be true. After co-registration, the random error of individual elevation changes can be estimated from the standard deviation of the differences over stable terrain. Although rare, an alternative to using stable terrain is to analyse two DEMs on glaciers (or a DEM with laser altimetry, i.e. ICESat) acquired at the same time (Berthier et al., 2012). In addition to the random error estimation, the error of the mean vertical bias adjustment should be included in the total error budget. This uncertainty may be estimated by the triangulation residual of the co-registration vectors (see e.g. Nuth et al., 2012) or through a "null" test if two DEMs acquired at the same time are available (Berthier et al., 2012). Slope distributions of the terrain and elevation blunders in the DEMs may affect these estimates and should also be considered. For error estimates on mean glacier elevation changes and subsequent volume change estimates, spatial autocorrelation of the elevation data must be considered (Kääb, 2008; Rolstad et al., 2009; Schiefer et al., 2007).

4. Glacier elevation changes from altimetry

4.1 Background and previous work

Satellite altimetry is an alternative technique for estimating glacier elevation changes. There are two basic approaches: (1) the repeat-track method is based on elevation differences between ground tracks of closely repeated satellite orbits (Legresy et al., 2006; Howat et al., 2008; Pritchard et al., 2009) and (2) the cross-over method is based on interpolated elevation differences at crossing points of ground tracks (Zwally et al. 1989, Wingham et al. 1998). The cross-over method offers the most accurate observation of elevation trends, because the calculation is less dependent upon spatial variations in topography. Data from past altimetry missions (ERS, Envisat, ICESat) are sparsely distributed in space due to constraints on the mission ground tracks, and are best suited to study averaged changes over large (>10^2 km^2)

areas (Nuth et al., 2010; Moholdt et al., 2010a and b; Kääb et al., 2012). In contrast, the CryoSat-2 satellite offers the potential for vastly superior spatial sampling due to the dense orbit ground track. For comparison, at a latitude of 60° the average separation of ICESat, ERS/Envisat, and CryoSat orbit crossing points is 175 km, 35 km, and 2 km, respectively.

Although repeat-track altimetry provides measurements of elevation change that are of inferior accuracy to those acquired by the cross-over method, the approach provides a far better spatial sampling because measurements are available in-between each cross-over point. Topographically corrected elevation differences can be obtained by several methods:

- triangulation between near repeat-tracks (Pritchard et al., 2009),
- fitting surface shapes to segments of near repeat ground tracks (Smith et al., 2009; Moholdt et al., 2010b; Sørensen et al., 2011; Flament et al., 2012; Schenk and Csatho, 2012),
- applying an external DEM for cross-track slope correction (Moholdt et al., 2010b), and
- differencing to a reference DEM and fitting a trend Rinne et al., 2011; Kääb et al., 2012).

The basic algorithms for the altimetric methods are well developed and have been widely reported in the literature (e.g. Zwally et al., 1989; Wingham et al., 1998; Shepherd et al., 2001; Shepherd and Wingham, 2007; Nuth et al., 2010; Moholdt et al., 2010b; Sørensen et al., 2011; Flament and Rémy, 2012). Some of these methods have been compared during the round robin of the project with the aim to select a 'best' performing algorithm. A validation activity using airborne altimetry has also been performed.

4.2 The round robin experiment

Test regions and methods

The test regions, Devon Ice Cap in Arctic Canada and Austfonna Ice Cap in Svalbard (see Fig. 1 for location), were chosen to cover glaciers with different surface characteristics and datasets. The exercise was based both on laser and radar altimetry data. Laser altimeter data were used as input to the different implementations of the repeat-track method, whereas radar altimeter data were used as input to the cross-over method. The laser data were acquired by the ICESat/GLAS instrument during the full acquisition period (2003-2009). In particular the GLA06 level 1B elevation product (release 33) was used. It provides surface elevations already corrected from geodetic and atmospheric effects and geolocated to the centre of the laser footprint. The radar data refer to the level 2 GDR version 2.1 acquired by the Envisat-RA2 altimeter during the period 2002-2010.

For the cross-over method, the dual cross-over algorithm reported in Wingham et al. (1998) was applied (XO-RepAlt). With this method, the elevation measurements from pairs of orbital cycles, acquired at two distinct times t_1 and t_2 were compared instead of combining ascending and descending tracks from a single orbital cycle. In this manner two pairs of elevations can be considered for computing the elevation change: the ascending track elevation measured during orbit cycle 1 at time t_1 and the descending track elevation measured during orbit cycle 2 at time t_2, as well as the ascending track measured at the orbit cycle 2 and the descending track measured at orbit cycle 1 (the elevation change during one orbit cycle is supposed to be negligible).

For the repeat-track method, three different algorithms were considered:

(1) the DEM-Projected correction method (DP-RT-RepAlt), described in Moholdt et al. (2010a and b), is based on the projection of one profile onto a neighbouring one by accounting for the cross-track slope using an external DEM; elevations are then compared at each DEM-projected point by linear interpolation between the two closest footprints in the other profile;

(2) the Rectangular Plane fitting method (RP-RT-RepAlt), described in detail by Moholdt et al. (2010b), is based on a least-squares regression technique that fits rectangular planes to segments of repeat-track data; for each plane the elevation change rate, supposed constant, is estimated; and

(3) the DEM Subtracting method (DS-RT-RepAlt), described in Ticconi et al. (2012), computes the difference between the altimetry measured elevations and the DEM elevations at each altimetry footprint location as determined from bilinear interpolation. Elevation differences are then grouped within the selected area, e.g. a pre-defined grid, and within different time seasons. Linear trends are then fitted to the data to estimate average elevation change rates.

For (1) and (3) the precision of the DEM is crucial for the quality of the results. Table 3 provides details about the data sets and the temporal coverage for each algorithm and test site.

Table 3

The aims of the round robin were the validation of different repeat-pass altimetry algorithms for product generation, and the selection of a 'best' performing algorithm. The validation of the derived elevation changes focused on:

(a) comparison of airborne elevation changes with satellite altimeter elevation changes,

(b) comparison of elevation changes derived from different sensors (e.g. radar vs. laser), and

(c) comparison of elevation changes derived from different algorithms (cross-over vs. repeat-track).

The validation strategy (a) ensures independence, since it is based on external data which have not been used during the generation of the elevation change products derived from satellite altimeter data. The validation strategy (b) provides two independent elevation change products to be compared, because even if the same algorithm has been used to create them, it has been applied on two different data sets acquired by two different sensors. The same applies for the validation strategy (c), which provides two independent elevation change products derived from two different algorithms to a data set acquired by the same sensor.

The validation criteria were based upon the computation of the root mean square error *(RMSE)* and the correlation coefficient (R). This has been applied to the comparisons (a), (b) and (c) described above. The limitation of the cross-over methods in terms of spatial coverage when compared with the repeat-track method was shown in Ticconi et al. (2012) for the Devon Ice Cap. The authors of that study compared the elevation changes obtained by the RP-RT-RepAlt technique applied on the full ICESat/GLAS archive (2003-2009) with the elevation changes obtained by XO-RepAlt using the Envisat radar altimeter data over the period 2002-2010. However, the small number of cross-over points made these results unsuitable for the comparison of the different algorithms. The comparison between the different repeat-track implementations is reported in Fig. 6. The left panel shows the comparison between the DS-RT-RepAlt and the RP-RT-RepAlt performed over Devon Ice Cap, whereas the right panel shows the comparison between the DP-RT-RepAlt and the RP-RT-RepAlt over Austfonna. The good correspondence expressed by an *RMSE* of 0.47 m/yr in the first case and 0.41 m/yr in the other indicates that the two DEM-based algorithms are almost equivalent.

Figure 6

The validation against airborne data was performed only over the Austfonna test site using the airborne data reported in Bamber et al. (2004). The repeated laser altimetry data were acquired in 1996 and 2002. Both airborne and ICESat surface elevations below 100 m were discarded from the analysis. Furthermore, the two data sets were separately averaged within elevation intervals of 100 m considering the entire ice cap. It appeared that the radar altimeter data were not properly measuring the elevations along the ice cap margin where slopes were steep. The reasons for this behaviour could be related to a large footprint and to time variation changes. Table 4 reports the average and the standard deviation values obtained over elevation intervals of 100 m for the methods applied at this test site, i.e. the DP-RT-RepAlt, the RP-RT-RepAlt and the XO-RepAlt algorithms. The last three columns report the absolute differences between the average values of the three algorithms and the average values of the airborne dataset, whose trends are also visualised in Fig. 7 as a function of the elevation. They show a similar tendency when elevation becomes greater than 300 m. For elevations below this value, a dissimilarity between the absolute differences can be noted when radar altimeter data are used, indicating that radar performs better in regions with moderate slope than in regions with high slopes like the ice margin. Fig. 8 shows the scatter-plots between the two repeat track algorithms used, i.e. the DP-RT-RepAlt and the RP-RT-RepAlt, against the cross-over method, i.e the XO-RepAlt. In both cases the RMSE is more than 1 m/yr and the correlation coefficient assumes a small value close to zero indicating that the there is no correlation between the two methods. This result can be explained by the fact that the number of cross-over points is relative small when compared with the elevation measurements used in the two repeat track algorithms.

Table 4

Figures 7 and 8

Round robin results and algorithm selection

The selection of the best performing algorithm was based on the following criteria:

- spatial and temporal density of satellite derived surface elevation changes
- absolute accuracy relative to validation data
- processing time and manual interaction

Table 5 reports the algorithm performance in terms of absolute accuracy. Table 6 summarises the overall performance of the tested algorithms in relation to the above selection criteria over the two test sites.

Tables 5 and 6

To sum up, the absolute difference has been used to compare the elevation change trends derived from the different altimetry algorithms. The root mean square error (*RMSE*) and correlation coefficiient *R* were computed to provide a quantitative analysis. The results showed that the DP-RT-RepAlt and the RP-RT-RepAlt algorithms had an *RMSE* of about 0.4 m/yr when compared with the airborne data, indicating a good agreement. The good agreement with airborne data is supported by the high *R* value (~0.73). In addition, the repeat track algorithms demonstrated a similar RMSE when inter-compared and a very high *R* value (0.89), indicating that they were almost equivalent.

5. Glacier velocity

5.1 Background and previous work

A large number of archived and upcoming optical and SAR satellite missions make it possible to operationally map and monitor glacier flow on a nearly global scale, providing unique glaciological information (Joughin et al., 2010; Rignot et al., 2011; Heid and Kääb, 2012a and b). Such knowledge will contribute to a better understanding of a wide range of processes related to glacier dynamics, for example glacier mass flux, flow modes and flow instabilities (e.g. surges), subglacial processes (e.g. erosion), supra- and intra-glacial mass transport, and the development of glacier lakes and associated hazards (Kääb et al., 2005). The comparison of the spatio-temporal variations of glacier velocities both within and between regions will improve understanding of climate change impacts (e.g. Scherler et al., 2011). In response to 2-3 decades of negative glacier mass balances, glacier surface velocity is currently slowing down in many mountain ranges (Heid and Kääb, 2012a and b; Span and Kuhn, 2003; Berthier and Vincent, 2012), a dynamic behaviour that in turn will also influence their response to future climate change. In this regard, mapping and monitoring glacier flow globally complements the possibilities for determination of glacier areas and volume changes described above.

The calculation of glacier velocity fields is possible with repeat optical satellite imagery (Scambos et al., 1992) and SAR data using speckle and/or feature tracking methods (Gray et al., 1998). They are usually called “image matching” in the optical domain and “offset-tracking” in the microwave domain, but we here use the term offset tracking for both optical and SAR data. Indeed, strictly speaking image matching refers only to the image correlation itself and does not include the required pre- and post-processing procedures. The suitable temporal baselines of the repeat data are subject to two fundamental constraints: (i) the displacements have to be statistically significant (i.e. have to be larger than the accuracy of the method); (ii) surface changes due to melt, deformation, snow fall, etc. over the measurement period have to be small enough so that corresponding intensity or phase features can be matched in both data sets. Typical baselines suitable for optical data are weeks to years whereas for SAR offset-tracking intervals of days to a few weeks are required. Interferometric techniques are not analysed here as they require a very short baseline (days) and are less suitable for operational and global-scale application (Fig. 9). However, SAR interferometry was widely used to determine flow velocities of ice sheets, where decorrelation due to a change of surface properties is less of a problem (e.g. Goldstein et al., 1993; Joughin et al., 1996; Rignot et al., 1997). To overcome signal decorrelation when using longer time intervals or analysing more rapidly changing temperate glaciers, offset-tracking procedures are largely adopted (Gray et al., 1998; Michel and Rignot, 1999; Derauw, 1999; Strozzi et al., 2002; Quincey et al., 2009; Rignot et al., 2011). Repeat optical satellite imagery from sensors such as SPOT, Terra ASTER and Landsat ETM+ pan were also widely applied to determine flow velocities of glaciers (e.g. Berthier et al., 2005; Herman et al., 2011; Kääb, 2005b; Kääb et al. 2006; Scherler et al., 2008 and 2011). Here we focus on Landsat data with 15 m spatial resolution (ETM+ pan), due mainly to the large spatial coverage of one scene, the huge archive available and the perspective of future missions with similar characteristics (e.g. Landsat 8, Sentinel-2). Data acquired by Envisat ASAR (C-Band), ALOS PALSAR (L-Band) and TerraSAR-X (X-Band) data were considered as microwave imagery for algorithm testing.

Figure 9

Despite their wide application, only a few systematic studies compared different algorithms and procedures for glacier surface velocity estimation based on repeat optical or microwave data. Starting with optical sensors, Heid and Kääb (2012a) compared a number of frequently used and already published matching algorithms. Despite differences in the results under conditions that are initially difficult, for instance in regions with low visual contrast, most algorithms are in principle able to measure displacements at sub-pixel precision. As most optical offset-tracking procedures rely on matching repeat orthoimages, errors in the sensor model, sensor orientation, and the DEM translate into lateral errors in the data to be matched and thus in the displacements obtained (see section 3). Leprince et al. (2007) developed a procedure to rigorously remove such effects and Debella-Gilo and Kääb (2011) analysed the effect of a locally adaptive way to determine the optimal size of matching templates, combined with finding suitable matching targets based on the image grey scale variations (image signal-to-noise ratio). Ahn and Howat (2011) applied normalised cross-correlation (NCC) to a large number of input image versions (e.g. channels, gradients, filtered versions, principle components) and a range of template sizes, to find the most probable displacement based on the resulting stack. Though computationally very expensive, this approach is locally adaptive in many geometric and radiometric respects. In the same direction Liu et al. (2012) propose a multi-scale matching process to overcome the dependence of the matching window size on the velocity. For SAR data, comparisons are related to optical versus SAR methods, the impact of the matching window size on the derived velocity (Huang and Li, 2011) or InSAR versus offset (or speckle) tracking methods (e.g. Joughin, 2002; Luckman et al., 2007).

In the round robin for the glacier velocity product different image matching algorithms for SAR and optical data were compared with robust and global-scale applications in mind. Test regions (cf. Fig. 1) were located in Iceland (Breidamerkurjökull, an outlet glacier of the Vatnajökull Ice Cap), High-Mountain Asia (Baltoro Glacier in the Karakoram), and Svalbard (Vestfonna Ice Cap). In the following sections, we describe the algorithms selected for generating the velocity product, including practical considerations during the pre- and post-processing stages.

5.2 Pre-processing for SAR and optical sensors

In the pre-processing step data import and quality checks (e.g. missing line detection for SAR data) are performed. The most crucial step is the accurate co-registration of the data to be matched (see section 3). Offsets were measured using the same algorithms as in the main processing (though often with different parameterisations, e.g. with a reduced sampling to decrease the computational effort) or using another algorithm and form the base of co-registration. A glacier mask and a DEM can be optionally employed to limit the search over stable ground and to compensate for the stereo offsets relevant for the range offset field, respectively. The slave (or search) image can be then either transformed to the geometry of the master (or reference) image or (e.g. polynomial) transformation parameters can be computed and applied to the matching results without transforming the images. The co-registration transformation has the advantage to make offset-tracking and other usages of the images easier, but increases the computational time and storage requirements and may introduce loss of information, even if this is marginal for SAR data.

A generic optical offset-tracking procedure for large-scale and frequent operational usage will have to be based on orthorectified data, as some data are, or will be only available in orthorectified form (Landsat, Sentinel-2) or because orthorectification within the tracking procedure will be difficult, e.g. due to instable sensor geometry (Leprince et al. 2007). As a result, the displacements are not necessarily the highest accuracy level theoretically achievable, but will rather be contaminated by propagated DEM errors, errors in the sensor model and sensor orientation, such as jitter (Scherler et al., 2008; Nuth and Kääb, 2011). Co-registration can in some cases partially reduce these influences empirically, but will in most cases be more useful for estimating the size of these effects and add them to the error budget of the displacements. As glacier thickness changes with time, it is important to determine off-glacier DEM errors only from data over stable ground.

5.3 Main Processing of satellite optical data

For the round robin we applied several image matching algorithms to the same data sets. For an internal algorithm test we selected from the six algorithms originally discussed in Heid and Kääb (2012a), two (1 and 2 in the list below) which are assumed to be beneficial for large-scale, operational offset-tracking and compared them to algorithms (3) and (4) applied by the external round robin participants:

(1) normalised cross-correlation (NCC) in the spatial domain (see details in Appendix),
(2) orientation correlation (CCF-O) in the frequency domain (see details in Appendix),
(3) a modified version of the GAMMA software (matching template 30 x 30 pixels, 5-pixel spacing) using in principle NCC for offset-tracking, but solved in the Fourier domain, and

(4) a modification of the Ahn and Howat (2011) method using NCC (matching template 31 x 31 pixels, 8-pixel spacing) but with sophisticated pre- and post-processing procedures.

The NCC method turns out to perform similar to the CCF-O in regions with good visual contrast (typically ablation areas, debris cover), but obtains fewer correct matches in regions with low visual contrast (Fig. 10; no close-ups of images are shown here for better illustrating variations of visual contrast). The Fourier methods (2) and (3) performed also similarly in regions of high visual contrast but fewer correct matches were obtained by (3) in regions of low visual contrast. This was expected since the method is based on NCC that has worse performance in low contrast regions. For regions in which the velocity gradients (strain rates) were large, the NCC (1) and the NCC with sophisticated pre- and postprocessing procedures (4) outperformed both of the Fourier methods tested. However with the pre-processing steps in (4), where a glacier mask is found by initial matching, some smaller glaciers, stagnant glacier fronts and large parts of the accumulation area, where the movement was slow, were neglected and unmatched.

Figure 10

Results with satellite optical data suggested that no single matching method clearly outperformed all other methods investigated under all circumstances, but rather that a set of two methods – e.g. (1) and (2) – should be combined depending on the image conditions and the glacier characteristics. These two algorithms were chosen for further development in Glaciers_cci. The algorithm evaluation further revealed that most algorithms and implementations were in principle able to achieve precisions in the sub-pixel range (e.g. if data taken from the same orbit were used).

5.4 Main Processing of satellite SAR data

The NCC algorithm is simple and robust and can also be applied to SAR data. Offsets are measured using rectangular windows that are m_1 x m_2 (range x azimuth) pixels in dimension at a set of positions in the scene. The locations may be uniformly distributed over the image frame but for deformation mapping at specific regions (i.e. glaciers) also can be selected for dense sampling. After global co-registration, the residual offsets should not be larger than a small fraction of the patch size that will be used for measuring the offset field. Typical values for m_1 and m_2 are in the range of 64 to 256 pixels depending on the noise level, sensor resolution and specific application. Generally these sizes correspond to 300 - 1000 m on the ground. Corresponding data patches are extracted from each single-look complex image (SLC) and are typically over-sampled by a factor of 2 or more using FFT interpolation to substantially improve the accuracy (Werner et al., 2005). The location of the maximum of the 2D correlation function yields the desired range and azimuth offsets. In order to obtain an accurate estimate of the correlation peak, the correlation function values over a (m_1 x m_2) region can be fitted using a bi-quadratic polynomial surface. The signal-to-noise ratio (*SNR*) of the offset measurement is obtained by taking the ratio of the peak value divided by the average correlation level outside the (m_1 x m_2) peak region. Typical values for m_1 and m_2 are on the order of 3. The implementation of the algorithms may vary significantly with regard to matching window sizes and oversampling factors and various pre- and post-processing routines may affect the quality of the results (Fig. 11). Offset tracking methods, even when implemented in the frequency domain using FFTs, are computationally expensive, and can take up to several hours on a single CPU, for a single SAR image frame, depending on window size, pixels spacing and oversampling factor. However, in principle each data patch can be processed in parallel, allowing for large gains in processing time when using parallelized code.

Figure 11

The accuracy of the cross-correlation algorithm was investigated in various aspects, including a formal description of the error terms (noise, stereo offsets, imperfectly compensated satellite orbit configurations, ionospheric effects), matching on stable ground (Fig. 12), inferring statistical errors on the difference of matching image 1 with image 2 with respect to the matching of image 2 with image 1, comparison against results from image data of equal or better resolution, and ground-based measurements from DGPS (Fig. 13). We finally estimated the reliability of the cross-correlation algorithm to return co-registration parameters on the order of 1/10th of a SAR image pixel. This corresponds for the ALOS PALSAR and TerraSAR-X data separated by a temporal interval of 46 and 11 days, respectively, to an accuracy of about 10 m/yr and for the Envisat ASAR data separated by a temporal interval of 35 days to an accuracy of about 20 m/yr. Outliers were frequent and required special attention during post-processing.

Figure 12

5.5 Post-processing

The matching algorithms do not directly provide perfect results. Errors and outliers cannot be avoided because of non-perfect image and ground conditions and have to be detected and filtered as much as possible in a post-processing step. The NCC algorithm provides, together with the offset with highest score, the correlation coefficient (*R*) or *SNR* of the resulting offset. These measures can directly be used to estimate the potential quality of a match, and filters based on *R* or *SNR* thresholds can be developed. Since *R* and *SNR*, however, depend not only on the quality of a match but also on the image texture, such filters are not strictly conclusive and should be used with care and only in combination with other post-processing measures. The resulting displacement field can be low-pass filtered (e.g. mean, median, Gaussian, etc.) to filter out individual outliers. Similar to a resolution pyramid, the raw displacements can be compared to a low-pass filtered version of the field and measurements marked as outliers when the difference exceed a given threshold on displacement magnitude and direction (Heid and Kääb, 2012a). This procedure is very successful over dense fields, but may fail where successful matches are only scattered, or where entire groups of displacements have a similar bias.

Geometric constraints such as maximum magnitude or direction sectors can be also used as filters (e.g. Skvarca et al., 2003). However, they are not very useful for large-scale applications including a number of glaciers with different speeds and orientations. Also, for instance, gradients in glacier velocities could be used to filter, but they are very different from region to region due to the large variety of glaciers. To filter the displacements based, for instance, on the assumption that glaciers flow down-slope is considered to be impossible globally, because the required accurate elevation models are not available in all glacierized regions. There are also physical reasons where this assumption does not simply hold, such as in confluence areas or regions where ice flow is controlled by subglacial topography. The comparison of results using different pre-processing techniques or using CCF-O and NCC results can also be useful in reducing erroneous measurements. Ahn and Howat (2011) showed that the (automated) comparison of results obtained using different pre-processing techniques can also be useful, in particular in reducing erroneous measurements. However, as the CCF-O has an inherent bi-directional gradient filter, comparison of its results to NCC results resembles to some extent the comparison of differently pre-processed images.

Finally, we would like to stress that glaciologically sound and useful glacier displacements can only be obtained when the automatic results undergo an expert check and, potentially, editing (similar to the acknowledged good practice in multispectral glacier mapping). Thus, the aim of displacement filters is to remove the obvious errors so that the analyst can focus on details that require glaciological expert judgement.

6. Summary and discussion

6.1 Glacier area

Deriving glacier outlines from multispectral (optical) satellite images is straightforward from any of the available algorithms as soon as images with minimal seasonal snow and cloud covers are chosen. Manually selecting and optimizing classification thresholds has the advantage of minimizing the workload for editing in the post-processing stage (e.g. in shadow regions), but differences in the mapped glacier area when using constant threshold values will be small for glaciers with only few regions in shadow. On the other hand, correction of debris-covered glacier regions remains a laborious task. Although further semi-automated methods have been proposed recently (e.g. Bhambri et al., 2011; Shukla et al., 2011; Atwoodet al., 2010; Frey et al., 2012; Racoviteanu and Williams, 2012) none are in a stage where the automatically-derived outlines have the required accuracy, i.e. manual corrections have to be applied in all cases. Nonetheless they provide valuable support for deciding where glacier outlines should be. Actually, this decision can even be difficult in the field even with support from geophysical techniques. For the time being it is suggested that it would be worthwhile to prepare illustrated guidelines for the analyst, showing where glacier margins are located in difficult cases with examples from glaciers all around the world. At best, such a document should be prepared by a larger community to have wider consensus.

As a general summary, we propose that

- the satellite scenes to be processed need to be carefully selected in regard to snow and cloud conditions (mosaicking might be necessary but requires accurate co-registration of the different images),
- automated methods are preferable to map the bare ice,

- the threshold values should be chosen in a region with shadow,
- correction of the debris-covered parts should consider all information available, for example results of an automatic algorithm, hillshades from DEMs, high-resolution imagery in Google Earth™ or similar tools such as the freely available OrbView images from USGS http://earthexplorer.usgs.gov/, discussion with colleagues, and following examples (e.g. analyses of outlines from the GLIMS database and the published literature) and guidelines (e.g. Racoviteanu et al., 2009).

6.2 Elevation change from DEM differencing

The first step towards automated DEM differencing would be the implementation of a universal co-registration algorithm. All of the here presented round-robin-tested automated approaches performed with similar accuracies but different efficiencies. In terms of universal application, we propose a co-registration algorithm based upon terrain slope and aspect that requires only 2-3 optimazation iterations and is applicable with non-continuous elevation data, for example, from ICESat. Other lessons learned from the round robin are that various software products have different importing routines for the same file format (i.e. Geotiff) affecting the pixel definition (pixel centre vs. corner) and leading to large co-registration errors (typically half a pixel size) if an algorithm implementation requires switching the software. Thus, an automated processing chain for DEM differences should be maintained within one software product.

Apart from these challenges, results from the round robin for co-registering DEMs showed that sub-pixel accuracies (typically 1/10th to 1/5th of the DEM pixel size) were achieved using the three tested automatic algorithms. Only the analytical method using slope/aspect worked well with non-continuous data, such as from ICESat and could be solved with a minimum of iterations. The analytical solution requires the availability of stable terrain, typically with a uniform distribution of aspects on steeper slopes. While stable terrain is present in the majority of the glacierized regions of the world, it may not work for regions without stable terrain and/or where only very low slope surfaces are available, as equation (1) is not defined for a zero slope. The vertical co-registration adjustment had the largest variability between the methods applied in the round robin (Table 2) and this might be related to the selection of stable terrain. Its characteristics might thus have large impacts on the co-registration parameters solved as well as for any error quantification based upon this terrain.

6.3 Elevation changes from altimetry

In regard to the comparison between the elevation changes derived with satellite altimetry and the airborne measurements performed over the Austfonna ice cap, the absolute differences obtained using the DP-RT-RepAlt, the RP-RT-RepAlt and the XO-RepAlt showed similar trends when the elevation became greater than 300 m. It appeared that due to the large footprint of the radar altimeter, it was not properly measuring the elevation at the margin of the ice cap where surface slopes are high. In addition, the repeat-track method applied to laser altimeter data provided estimates of ice cap elevation change with greater accuracy than the cross-over method applied to radar altimeter (Table 5). Table 7 summarises the overall performance of the tested algorithms in relation to the selection criteria described. Based on these results, and when an external DEM is available, the DS-RT-RepAlt and the DP-RT-RepAlt are the only ones applicable for ICESat laser altimetry at mid to low latitudes because of the large cross-track spacing between repeat-tracks of up to several kilometres (Kääb et al., 2012). The two algorithms differ only in the manner of computing the elevation trend. The DS-RT-RepAlt is based on fitting a linear trend, whereas the DP-RT-RepAlt is based on a point by point comparison. Hence, for the scope of the CCI project, the DS-RT-RepAlt method applied to laser altimeter data has been selected as the reliable technique for developing satellite-based trend determination of elevation changes. The selected repeat-track algorithm might also be applicable to the Cryosat-2 radar altimeter data, which are characterised by a smaller footprint size compared to conventional radar altimeters. Being the first satellite equipped with a SAR interferometric altimeter, the sensor can point down to the location of the echo on sloping surfaces found around glaciers and ice caps.

Table 7

6.4 Glacier velocity

Results for glacier velocity measurement using satellite optical data suggested that no individual matching method clearly outperformed all other methods investigated under all circumstances, but rather that a set of, for instance, two methods – e.g. the NCC and the CCF-O – should be combined depending on the image conditions and the glacier characteristics. Results from the SAR round robin algorithm intercomparison demonstrated that, for the provided datasets and with temporal baselines >11 days, the normalized cross-correlation of chips in amplitude SAR images performed better compared to phase-based SAR methods (SAR interferometry and multiple-aperture interferometry, see Fig. 9), in particular regarding its wider application to different glaciers and SAR data. Accuracy of offset-tracking using high to very-high resolution SAR data with a time interval of one orbital cycle are about 10 m/yr, similar to the accuracy for medium-resolution optical satellite imagery (e.g. Landsat ETM+ pan) that is on the order of 15 m/year for images acquired one year apart. However, there will be outliers that have lower accuracies. These can occur due to:

- poor image co-registration and orthoprojection error (can be checked over stable terrain);
- sub-pixel geometric sensor noise level (usually larger than algorithm precision);
- surface changes and transformations, e.g. influence of different illuminations and shift of surface features;
- mismatches due to similar but not corresponding features, e.g. self-similar ogives, crevasses or seracs, with errors of many pixels possible;
- inability of post-processing procedures to eliminate measurement noise and mismatches.

7. Conclusions and Perspectives

We have described methods and algorithms for deriving three glacier related products (area, elevation change, flow velocity) from a variety of space-borne sensor types (optical and microwave imagers or altimeters). They generally provide complementary information and are thus particularly useful for glaciological research when combined. The algorithms presented were selected for data production in the Glaciers_cci project after careful evaluation and comparison with alternative methods. In regard to a more general data processing workflow, all methods selected have also product-specific peculiarities. For the glacier area product the mapping algorithm is very simple (band ratio with threshold) and the manual editing of wrong classifications (debris cover) in the post-processing stage drives the accuracy of the final product. The quality of the elevation change product (from DEM differencing) depends on the quality of the input DEMs, on the use of a single software processing chain for co-registration (as pixel coordinates can be interpreted differently), and on the post-processing stage (e.g., removal of altitudinal or other biases). The processing of the velocity and elevation change (from altimetry) products is largely automatic, but the algorithms are much more complex and the computational resources required are thus much higher. In all cases product quality also depends on the quality of external data such as a high-quality DEM, which is not yet available for all high-mountain regions of the world. Moreover, if more than one algorithm can be applied (e.g. for velocity), the best choice often depends on the specific characteristics of the investigated region and might have to be tested. For ice velocities the major differences between different processing schemes may also stem from different implementations, pre- and post-processing steps, which should thus be carefully selected. Velocity measurements from repeat satellite optical and SAR sensors have a large potential to be accomplished automatically further arriving at robust global-scale products. More detailed information on algorithms, work flows and product generation is available from the documents on the Glaciers_cci website (http://www.esa-glaciers-cci.org/). With the recently launched (Cryosat-2, TanDEM-X, Landsat 8) or planned (Sentinels 1 and 2) satellite missions and the commitment to free data distribution by space agencies, the contribution of space-borne sensors to glacier monitoring will play an increasing role in the future.

Acknowledgements

This study was funded by the ESA project Glaciers_cci (4000101778/10/I-AM). We acknowledge the helpful comments to the paper by S. Plummer and the helpful and constructive reviews of three anonymous reviewers.

Appendix

The NCC is given by:

$$NCC(i,j) = \frac{\sum_{kl}(s(i+k,j+1)-\mu_s)(r(k,l)-\mu_r)}{\sqrt{\sum_{k,l}(s(i+k,j+1)-\mu_s)^2 \sum_{k,l}(r(k,l)-\mu_r)^2}}$$

where (i,j) indicates the position in the search area, (k,l) the position in the reference area, r the pixel value of the reference chip, s the pixel value of the search chip, μ_r the average pixel value of the reference chip and μ_s the average pixel value of the search chip.

In CCF-O, orientation images are first derived from the original images. Taking f as the image at time t = 1 and g as the image at time t = 2, the orientation images f_o and g_o are created from:

$$f_o(x,y) = sgn\left(\frac{\partial f(x,y)}{\partial x} + i\frac{\partial f(x,y)}{\partial y}\right)$$

$$g_o(x,y) = sgn\left(\frac{\partial g(x,y)}{\partial x} + i\frac{\partial g(x,y)}{\partial y}\right)$$

$$\text{where } sgn(x) = \begin{cases} 0 & \text{if } |x| = 0 \\ \frac{x}{|x|} & \text{otherwise} \end{cases}$$

where sgn is the signum function, i is the complex imaginary unit, and the new images f_0 and g_0 are complex, they are matched using cross-correlation:

$$\mathrm{CC}(i,j) = \mathrm{IFFT}\left(F_0(u,v)G_0^*(u,v)\right)$$

Here $F_0(u,v)$ is the Fast Fourier Transform (FFT) of the matching window from the image at time t = 1, $G_0(u,v)$ is the FFT of the matching window from the image at time t = 2, * denotes the complex conjugated and IFFT is the Inverse Fast Fourier Transform.

References

Ahn, Y. & Howat, I. M. (2011). Efficient automated glacier surface velocity measurement from repeat images using multi-image/multichip and null exclusion feature tracking. IEEE Transactions on Geoscience and Remote Sensing, 49(8), 2838-2846.

Albert, T. H. (2002). Evaluation of remote sensing techniques for ice-area classification applied to the tropical Quelccaya Ice Cap, Peru. Polar Geography, 26(3), 210-226.

Andreassen, L. M., Paul, F., Kääb, A. & Hausberg, J. E. (2008). Landsat-derived glacier inventory for Jotunheimen, Norway, and deduced glacier changes since the 1930s. The Cryosphere, 2, 131-145.

Aniya, M., Sato, H., Naruse, R., Skvarca, P. & Casassa, G. (1996). The use of satellite and airborne imagery to inventory outlet glaciers of the Southern Patagonia Icefield, South America. Photogrammetric Engineering and Remote Sensing, 62, 1361 - 1369.

Arendt, A. & 77 others (2012). Randolph glacier inventory [v2.0]: A dataset of global glacier outlines. GLIMS Technical report, 35 pp. Online at: http://www.glims.org/RGI, Global Land Ice Measurements from Space, Boulder, Colorado, USA.

Atwood, D., Meyer, F. & Arendt, A. (2010). Using L-band SAR coherence to delineate glacier extent. Canadian Journal of Remote Sensing, 36, S186-S195.

Bajracharya, S.R. & B.R. Shrestha (Eds.) (2011). The status of glaciers in the Hindu Kush-Himalayan Region, ICIMOD, Kathmandu.

Bamber J, Krabill W., Raper V. & Dowdeswell, J. (2004). Anomalous recent growth of part of a large Arctic ice cap: Austfonna, Svalbard. Geophysical Research Letters, 31, L12402.

Bayr, K. J., Hall, D. K. & Kovalick, W. M. (1994). Observations on glaciers in the eastern Austrian Alps using satellite data. International Journal of Remote Sensing, 15(9), 1733-1742.

Berthier, E. & Vincent, C. (2012). Relative contribution of surface mass balance and ice flux changes to the accelerated thinning of the Mer de Glace (Alps) over 1979-2008. Journal of Glaciology, 58(209), 501-512.

Berthier, E., Vadon, H., Baratoux, D., Arnaud, Y., Vincent, C., Feigl, K. L., Rémy, F. & Legresy, B. (2005). Surface motion of mountain glaciers derived from satellite optical imagery. Remote Sensing of Environment, 95, 14-28.

Berthier, E., Arnaud, Y., Vincent, C., & Rémy, F. (2006). Biases of SRTM in high-mountain areas: Implications for the monitoring of glacier volume changes. Geophysical Research Letters, 33, L08502.

Berthier, E., Arnaud, Y., Kumar, R., Ahmad, S., Wagnon, P. & Chevallier, P. (2007). Remote sensing estimates of glacier mass balances in the Himachal Pradesh (Western Himalaya, India). Remote Sensing of Environment, 108(3), 327-338.

Berthier, E., Schiefer, E., Clarke, G. K. C., Menounos, B. & Rémy, F. (2010). Contribution of Alaskan glaciers to sea-level rise derived from satellite imagery. Nature Geoscience, 3(2), 92-95.

Berthier, E., Scambos, T. A. & Shuman, C. A. (2012). Mass loss of Larsen B tributary glaciers (Antarctic Peninsula) unabated since 2002. Geophysical Research Letters, 39(13), L13501.

Bhambri, R., Bolch, T. & Chaujar, R. K. (2011). Automated mapping of debris-covered glaciers in the Garhwal Himalayas using ASTER DEMs and multi-spectral data. International Journal of Remote Sensing, 32(23), 8095-8119.

Bolch, T., Buchroithner, M., Pieczonka, T. & Kunert, A. (2008). Planimetric and volumetric glacier changes in the Khumbu Himal, Nepal, since 1962 using Corona, Landsat TM and ASTER data. Journal of Glaciology, 54, 592-600.

Bolch, T., Menounos, B., Wheate, R. (2010). Landsat-based glacier inventory of western Canada, 1985-2005. Remote Sensing of Environment, 114(1), 127-137.

Bolch, T., Pieczonka, T., & Benn, D.I. (2011). Multi-decadal mass loss of glaciers in the Everest area (Nepal, Himalaya) derived from stereo imagery. The Cryosphere, 5, 349-358.

Bolch, T., Sandberg Sørensen, L., Simonssen, S.B., Mölg, N., Machguth, H., Rastner, P., & Paul, F. (2013). Mass loss of Greenland's glaciers and ice caps 2003-2008 revealed from ICESat laser altimetry data. Geophys. Res. Lett., 40.

Cox, L. H. & March, R. S. (2004). Comparison of geodetic and glaciological mass-balance techniques, Gulkana Glacier, Alaska, USA. Journal of Glaciology, 50(170), 363-370.

Debella-Gilo, M. & Kääb, A. (2011). Locally adaptive template sizes in matching repeat images of Earth surface mass movements. ISPRS Journal of Photogrammetry and Remote Sensing, 69, 10-28.

Derauw, D. (1999). DInSAR and coherence tracking applied to glaciology: The example of Shirase Glacier. Proceedings FRINGE'99, Liège, Belgium.

Dozier, J. (1989). Spectral signature of alpine snow cover from Landsat 5 TM. Remote Sensing of Environment, 28, 9-22.

Finsterwalder, R. (1954). Photogrammetry and glacier research with special reference to glacier retreat in the eastern Alps. Journal of Glaciology, 2(15), 306-314.

Flament, T. & Rémy, F. (2012). Dynamic thinning of Antarctic glaciers from along-track repeat radar altimetry. Journal of Glaciology, 58(211), 830–840.

Frey, H., Paul, F. & Strozzi, T. (2012). Compilation of a glacier inventory for the western Himalayas from satellite data: Methods, challenges and results. Remote Sensing of Environment, 124, 832-843.

Fricker, H. A., Borsa, A., Minster, B., Carabajal, C., Quinn, K. & Bills, B. (2005). Assessment of ICESat performance at the Salar de Uyuni, Bolivia. Geophysical Research Letters, 32, L21S06.

Gardelle, J., Berthier, E. & Arnaud, Y. (2012a). Correspondence: Impact of resolution and radar penetration on glacier elevation changes computed from DEM differencing. Journal of Glaciology, 58(208), 419-422.

Gardelle, J., Berthier, E. & Arnaud, Y. (2012b). Slight mass gain of Karakoram glaciers in the early twenty-first century. Nature Geoscience, 5(5), 322-325.

Gardner, A. S., Moholdt, G., Wouters, B., Wolken, G. J., Burgess, D.O., Sharp, M. J., Cogley, J. G., Braun, C. & Labine, C. (2011). Sharply increased mass loss from glaciers and ice caps in the Canadian Arctic Archipelago. Nature, 473(7347), 357-360.

Gjermundsen, E. F., Mathieu, R., Kääb, A., Chinn, T., Fitzharris, B. & Hagen, J. O. (2011). Assessment of multispectral glacier mapping methods and derivation of glacier area changes, 1978-2002, in the central Southern Alps, New Zealand, from ASTER satellite data, field survey and existing inventory data. Journal of Glaciology, 57(204), 667-683.

Goldstein R., Engelhardt, H., Kamb, B. & Frolich, R. (1993). Satellite radar interferometry for monitoring ice sheet motion: application to an antarctic ice stream. Science, 262(5139),1525-30.

Gourmelen, N., Kim, S. W., Shepherd, A., Park, J. W., Sundal, A. V. & Bjornsson, H. (2011). Ice velocity determined using conventional and multiple-aperture InSAR. Earth and Planetary Science Letters, 307, 156-160.

Gray, L., Mattar, K. & Vachon, P. (1998). InSAR results from the RADARSAT Antarctic mapping mission: Estimation of glacier motion using a simple registration procedure. Proceedings. IGARSS'98, Seattle, WA.

Gruen, A. & Akca, D. (2005). Least squares 3D surface and curve matching. ISPRS Journal of Photogrammetry and Remote Sensing, 59(3), 151-174.

Hall, D. K., Ormsby, J. P., Bindschadler, R. A. & Siddalingaiah, H. (1987). Characterization of snow and ice zones on glaciers using Landsat Thematic Mapper data, Annals of Glaciology, 9, 104-108.

Haug, T., Kääb, A. & Skvarca, P. (2010). Monitoring ice shelf velocities from repeat MODIS and Landsat data - a method study on the Larsen similar to C ice shelf, Antarctic Peninsula, and 10 other ice shelves around Antarctica. Cryosphere, 4(2), 161-178.

Heid T. & Kääb A. (2012a). Evaluation of existing image matching methods for deriving glacier surface displacements globally from optical satellite imagery. Remote Sensing of Environment, 118, 339-355.

Heid T. & Kääb A. (2012b). Repeat optical satellite images reveal widespread and long term decrease in land-terminating glacier speeds. The Cryosphere, 6, 467-478.

Herman, F., Anderson, B. & Leprince, S. (2011). Mountain glacier velocity variation during a retreat/advance cycle quantified using sub-pixel analysis of ASTER images. Journal of Glaciology, 57(202), 197-207.

Howat, I. M., Smith, B. E., Joughin, I. & Scambos, T. A. (2008). Rates of southeast Greenland ice volume loss from combined ICESat and ASTER observations. Geophysical Research Letters, 35, L17505.

Huang, L. & Li, Z. (2011). Comparison of SAR and optical data in deriving glacier velocity with feature tracking. International Journal of Remote Sensing, 32(10), 2681-2698.

IGOS (2007). Integrated Global Observing Strategy Cryosphere theme report - For the monitoring of our environment from space and from Earth. Geneva: World Meteorological Organization. WMO/TD-No. 1405, 100 pp.

Jacobs, J. D., Simms, E. L. & Simms, A. (1997). Recession of the southern part of Barnes Ice Cap, Baffin Island, Canada, between 1961 and 1993, determined from digital mapping of Landsat TM. Journal of Glaciology, 43, 98-102.

Joerg, P. C., Morsdorf, F. & Zemp, M. (2012). Uncertainty assessment of multi-temporal airborne laser scanning data: A case study on an Alpine glacier. Remote Sensing of Environment, 127, 118-129.

Johannesson, T., Raymond, C. & Waddington, E. D. (1989). Time-scale for adjustment of glaciers to changes in mass balance. Journal of Glaciology, 35(121), 355-369.

Joughin, I. (2002). Ice-sheet velocity mapping: a combined interferometric and speckle-tracking approach. Annals of Glaciology, 34, 195-201.

Joughin, I., Tulaczyk, S., Fahnestock, M. & Kwok, R. (1996). A mini-surge on the Ryder Glacier, Greenland, observed by satellite radar interferometry. Science, 274, 228-230.

Joughin, I., Kwok, R. & Fahnestock M. (1998). Interferometric estimation of three-dimensional ice-flow using ascending and descending passes. IEEE Trans. Geosci. Remote Sensing, 36, 25-37.

Joughin, I., B. Smith, I. Howat, T. Scambos and T. Moon (2010). Greenland flow variability from ice-sheet-wide velocity mapping. Journal of Glaciology, 56 (197), 415-430.

Kääb, A. (2005a). Remote Sensing of Mountain Glaciers and Permafrost Creep. Schriftenreihe Physische Geographie, Geographisches Institut der Universität Zürich, 48, 266 pp.

Kääb, A. (2005b). Combination of SRTM3 and repeat ASTER data for deriving alpine glacier flow velocities in the Bhutan Himalaya. Remote Sensing of Environment, 94(4), 463-474.

Kääb A. (2008). Glacier volume changes using ASTER satellite stereo and ICESat GLAS laser altimetry. A test study on Edgeøya, Eastern Svalbard. IEEE Transactions on Geoscience and Remote Sensing, 46 (10), 2823-2830.

Kääb, A., Huggel, C., Paul, F., Wessels, R., Raup, B., Kieffer, H., & Kargel, J. (2003). Glacier Monitoring from ASTER Imagery: Accuracy and Applications. EARSeL eProceedings, 2, 43-53.

Kääb, A., Huggel, C., Fischer, L., Guex, S., Paul, F., Roer, I., Salzmann, N., Schlaefli, S., Schmutz, K., Schneider, D., Strozzi, T. & Weidmann, W. (2005). Remote sensing of glacier- and permafrost-related hazards in high mountains: an overview. Natural Hazards and Earth System Science, 5(4), 527-554.

Kääb, A., Lefauconnier, B. & Melvold, K. (2006). Flow field of Kronebreen, Svalbard, using repeated Landsat 7 and ASTER data. Annals of Glaciology, 42(1), 7-13.

Kääb A., Berthier, E., Nuth, C., Gardelle, J. & Arnaud, Y. (2012). Contrasting patterns of early twenty-first-century glacier mass change in the Himalayas. Nature, 488(7412), 495-498.

Kargel, J. S. & 16 others (2005). Multispectral imaging contributions to Global Land Ice Measurements from Space. Remote Sensing of Environment, 99, 187-219.

Kargel, J. S. & 15 others (2012). Greenland's shrinking ice cover: ″fast times″ but not that fast. The Cryosphere, 6, 533-537.

Kaser, G., Cogley, J. G., Dyurgerov, M. B., Meier, M. F. & Ohmura, A. (2006). Mass balance of glaciers and ice caps: Consensus estimates for 1961-2004. Geophys. Res. Lett., 33, L19501.

Korona, J., Berthier, E., Bernard, M., Rémy, F. & Thouvenot, E. (2009). SPIRIT. SPOT 5 stereoscopic survey of Polar Ice: Reference Images and Topographies during the fourth International Polar Year (2007-2009). ISPRS Journal of Photogrammetry and Remote Sensing, 64(2), 204-212.

Kunz, M., King, M. A., Mills, J. P., Miller, P. E., Fox, A. J., Vaughan, D. G. & Marsh, S. H. (2012). Multi-decadal glacier surface lowering in the Antarctic Peninsula. Geophysical Research Letters, 39, L19502.

Larsen, C. F., Motyka, R. J., Arendt, A. A., Echelmeyer, K. A. & Geissler, P. E. (2007). Glacier changes in southeast Alaska and northwest British Columbia and contribution to sea level rise. Journal of Geophysical Research-Earth Surface, 112(F1), F01007.

Le Bris, R., Paul, F., Frey, H. & Bolch, T. (2011). A new satellite-derived glacier inventory for western Alaska. Annals of Glaciology, 52(59), 135-143.

Legresy, B., Rémy, F. & Blarel, F. (2006). Along track repeat altimetry for ice sheets and continental surface studies. In: Proceedings of the Symposium on 15 years of Progress in Radar Altimetry, Venice, Italy, 13-18 March 2006 [Danesy, D. (ed.)]. ESA-SP614, Paper 181, European Space Agency Publications Division, Noordwijk, The Netherlands, 4 pp.

Lemke, P., Ren, J., Alley, R., Allison, I., Carrasco, J., Flato, G., Fujii, Y., Kaser, G., Mote, P. Thomas, R. & Zhang, T. (2007). Observations: change in snow, ice and frozen ground. Climate Change 2007: The Physical Science Basis. Contribution of Working Group I to the Fourth Assessment Report of the Intergovernmental Panel on Climate Change, S. Solomon, D. Qin, M. Manning, Z. Chen, M. Marquis, K.B. Averyt, M. Tignor & H.L. Miller, Eds., Cambridge University Press, Cambridge, 337-384.

Leprince, S., Barbot, S., Ayoub, F. and Avouac, J.-P. (2007). Automatic and Precise Orthorectification, Coregistration, and Subpixel Correlation of Satellite Images, Application to Ground Deformation Measurements. Geoscience and Remote Sensing, IEEE Transactions, 45, 1529-1558.

Liu, H. X., Wang, L., Tang, S. J. & Jezek, K. C. (2012). Robust multi-scale image matching for deriving ice surface velocity field from sequential satellite images. International Journal of Remote Sensing, 33(6) 1799-1822.

Luckman, A., Quincey, D. & Bevan, S. (2007). The potential of satellite radar interferometry and feature tracking for monitoring flow rates of Himalayan glaciers. Remote Sensing of Environment, 111, 172-181.

Malenovsky, Z., Rott, H., Cihlar, J., Schaepman, M. E., García-Santos, G., Fernandes, R. and Berger, M. (2012). Sentinels for science: Potential of Sentinel-1, -2, and -3 missions for scientific observations of ocean, cryosphere, and land. Remote Sensing of Environment 120, 91-101.

Manley, W. F. (2008). Geospatial inventory and analysis of glaciers: a case study for the eastern Alaska Range. In Williams, R.S., Jr. and J.G. Ferrigno, Eds. Satellite image atlas of glaciers of the world. USGS Professional Paper, 1386-K, K424-K439.

McVicar, T.R. and Körner, C. (2013) On the use of elevation, altitude and height in the ecological and climatology literature. Oecologia. 171(2), 335-337.

Miller, P. E., Kunz, M., Mills, J. P., King, M. A., Murray, T., James, T. D. & Marsh, S. H. (2009). Assessment of Glacier Volume Change Using ASTER-Based Surface Matching of Historical Photography. IEEE Transactions On Geoscience and Remote Sensing, 47(7), 1971-1979.

Miller, P. E., Mills, J., Edwards, S., Bryan, P., Marsh, S., Mitchell, H. & Hobbs, P. (2008). A robust surface matching technique for coastal geohazard assessment and management. ISPRS Journal of Photogrammetry and Remote Sensing, 63(5), 529-542.

Michel, R. & Rignot, E. (1999). Flow of Glaciar Moreno, Argentina, from repeat-pass Shuttle Imaging Radar images: Comparison of the phase correlation method with radar interferometry. Journal of Glaciology, 45(149), 93–100.

Moholdt, G., Hagen, J. O., Eiken, T. & Schuler, T. V. (2010a). Geometric changes and mass balance of the Austfonna ice cap, Svalbard. The Cryosphere, 4, 21-34.

Moholdt, G., Nuth, C., Hagen, J. O. & Kohler, J. (2010b). Recent elevation changes of Svalbard glaciers derived from ICESat laser altimetry. Remote Sensing of Environment, 114(11), 2756-2767.

Mohr, J. J., Reeh, N. & Madsen, S. (1998). Three-dimensional glacial flow and surface elevation measured with radar interferometry. Nature, 391, 273–276.

Nuth, C. & Kääb, A. (2011). Co-registration and bias corrections of satellite elevation data sets for quantifying glacier thickness change. The Cryosphere, 5(1), 271-290.

Nuth, C., Moholdt, G., Kohler, J., Hagen, J. O. & Kääb, A. (2010). Svalbard glacier elevation changes and contribution to sea level rise. Journal of Geophysical Research-Earth Surface, 115.

Nuth, C., Schuler, T. V., Kohler, J., Altena, B. & Hagen, J. O. (2012). Estimating the long-term calving flux of Kronebreen, Svalbard, from geodetic elevation changes and mass-balance modelling. Journal of Glaciology, 58(207), 119-133.

Østrem, G. (1975). ERTS - 1 data in glaciology - an effort to monitor glacier mass balance from satellite imagery, Journal of Glaciology, 15, 403-415.

Paul, F. (2002). Changes in glacier area in Tyrol, Austria, between 1969 and 1992 derived from Landsat 5 TM and Austrian Glacier Inventory data. International Journal of Remote Sensing, 23(4), 787-799.

Paul, F. (2008). Calculation of glacier elevation changes with SRTM: is there an elevation-dependent bias? Journal of Glaciology, 54(188), 945-946.

Paul, F. & Kääb, A. (2005). Perspectives on the production of a glacier inventory from multispectral satellite data in the Canadian Arctic: Cumberland Peninsula, Baffin Island. Annals of Glaciology, 42, 59-66.

Paul, F. & Haeberli, W. (2008). Spatial variability of glacier elevation changes in the Swiss Alps obtained from two digital elevation models. Geophysical Research Letters, 35, L21502.

Paul, F. & Hendriks, J. (2010). Optical remote sensing of glaciers. In: Pellikka, P. & Rees, W.G (Eds.)., Remote Sensing of Glaciers. CRC Press, Taylor and Francis, Leiden, 137-152.

Paul, F., Kääb, A., Maisch, M., Kellenberger, T. W. & Haeberli, W. (2002). The new remote-sensing-derived Swiss glacier inventory: I. Methods. Annals of Glaciology, 34, 355-361.

Paul, F., Huggel, C., Kääb, A. & Kellenberger, T. (2003). Comparison of TM-derived glacier areas with higher resolution data sets. EARSeL Workshop on Remote Sensing of Land Ice and Snow, Bern, 11.-13.3.2002. EARSeL eProceedings, 2, 15-21.

Paul, F., Barry, R., Cogley, J.G., Frey, H., Haeberli, W., Ohmura, A., Ommanney, C. S. L., Raup, B. H., Rivera, A. & Zemp, M. (2009). Recommendations for the compilation of glacier inventory data from digital sources. Annals of Glaciology, 50(53), 119-126.

Paul, F., Frey, H. & Le Bris, R. (2011). A new glacier inventory for the European Alps from Landsat TM scenes of 2003: Challenges and results. Annals of Glaciology, 52(59), 144-152.

Paul, F. & 19 others (2013). On the accuracy of glacier outlines derived from remote sensing data. Annals of Glaciology, 54(63), 171-182.

Pohjola, V. A., Christoffersen, P., Kolondra, L., Moore, J. C., Pettersson, R., Schäfer, M., Strozzi, T. & Reijmer, C.H. (2011). Spatial distribution and change in the surface ice-velocity field of Vestfonna ice cap, Nordaustlandet, Svalbard, 1995–2010 using geodetic and satellite interferometry data. Geografiska Annaler: Series A, Physical Geography, 93, 323-335.

Pritchard, H. D., Arthern, R. J. ,Vaughan, D. G. & Edwards, L. A. (2009). Extensive dynamic thinning on the margins of the Greenland and Antarctic ice sheets. Nature, 461, 971-975.

Quincey, D.J., Copland, L., Mayer, C., Bishop, M., Luckman, A. and Belò, M. (2009). Ice velocity and climate variations for Baltoro Glacier, Pakistan. Journal of Glaciology, 55(194), 1061-1071.

Racoviteanu, A. & Williams, M. W. (2012). Decision tree and texture analysis for mapping debris-covered glaciers in the Kangchenjunga area, Eastern Himalaya. Remote Sensing, 4, 3078-3109.

Racoviteanu, A. E., Williams, M. W. & Barry, R. G. (2008). Optical remote sensing of glacier characteristics: A review with focus on the Himalaya. Sensors, 8, 3355-3383.

Racoviteanu, A. E, Paul, F., Raup, B., Khalsa, S. J. S. & Armstrong, R. (2009). Challenges in glacier mapping from space: recommendations from the Global Land Ice Measurements from Space (GLIMS) initiative. Annals of Glaciology, 50(53), 53-69.

Rastner, P., Bolch, T., Mölg, N., Machguth, H. & Paul, F. (2012). The first complete glacier inventory for the whole of Greenland. The Cryosphere, 6, 1483-1495.

Raup, B. H. & Kahlsa, S. J. S. (2007). GLIMS Analysis Tutorial. NSIDC, Boulder, Colorado. (http://www.glims.org/MapsAndDocs/assets/GLIMS_Analysis_Tutorial_a4.pdf)

Raup, B. H., Racoviteanu, A., Khalsa, S. J. S., Helm, C., Armstrong, R. & Arnaud, Y. (2007b). The GLIMS Geospatial Glacier Database: a new tool for studying glacier change. Global and Planetary Change, 56, 101-110.

Rignot, E., Gogineni, S., Krabill, W. & Ekholm, S. (1997). North and Northeast Greenland ice discharge from satellite radar interferometry. Science, 276, 934–937.

Rignot, E., Mouginot, J. & Scheuchl, B. (2011). Ice Flow of the Antarctic Ice Sheet. Science, 333(6048). 1427-1430.

Rinne, E. J., Shepherd, A., Palmer, S., van den Broeke, M. R., Muir, A., Ettema, J., & Wingham, D. (2011). On the recent elevation changes at the Flade Isblink Ice Cap, northern Greenland. 2011. Journal of Geophysical Research, 116, F03024.

Rodriguez, E., Morris, C. S. & Belz, J. E. (2006). A global assessment of the SRTM performance. Photogrammetric Engineering and Remote Sensing, 72(3), 249-260.

Rolstad, C., Haug, T. & Denby, B. (2009). Spatially integrated geodetic glacier mass balance and its uncertainty based on geostatistical analysis: application to the western Svartisen ice cap, Norway. Journal of Glaciology, 55, 666-680.

Rott, H. (1976). Analyse der Schneeflächen auf Gletschern der Tiroler Zentralalpen aus Landsat Bildern. Zeitschrift für Gletscherkunde und Glazialgeologie, 12, 1-28.

Rott, H. (1994). Thematic studies in alpine areas by means of polarimetric SAR and optical imagery. Advances in Space Research, 14, 217-226.

Rott, H. & Markl, G. (1989). Improved snow and glacier monitoring by the Landsat Thematic Mapper, Proceedings of a workshop on Landsat Themaic Mapper applications, ESA, SP-1102, 3-12.

Scambos, T., Dutkiewicz, M. J., Wilson, J. C. & Bindschadler, R. A. (1992). Application of image cross-correlation to the measurement of glacial velocity using satellite image data. Remote Sensing of Environment, 42, 177-186.

Schenk, T. & Csatho, B. (2012). A New Methodology for Detecting Ice Sheet Surface Elevation Changes From Laser Altimetry Data. IEEE Transactions on Geoscience and Remote Sensing, 50(9), 3302-3316.

Scherler, D., Leprince, S. & Strecker, M. R. (2008). Glacier-surface velocities in alpine terrain from optical satellite imagery - Accuracy improvement and quality assessment. Remote Sensing of Environment, 112(10), 3806-3819.

Scherler, D., Bookhagen, B. & Strecker, M. R. (2011). Spatially variable response of Himalayan glaciers to climate change affected by debris cover. Nature Geoscience, 4(3), 156-159.

Schiefer, E., Menounos, B. & Wheate, R. (2007). Recent volume loss of British Columbian glaciers, Canada. Geophys. Res. Lett., 34, L16503.

Schiefer, E., Menounos, B., & Wheate, R.D. (2008). An inventory and morphometric analysis of British Columbia glaciers, Canada. Journal of Glaciology, 54, 551-560.

Shangguan, D., Liu, SY., Ding, YJ., Ding, LF., Xu, JL. & Jing, L. (2009). Glacier changes during the last forty years in the Tarim Interior River basin, northwest China. Progress in Natural Science, 19(6), 727-732.

Shepherd, A. & Wingham, D. J. (2007). Recent sea-level contributions of the Antarctic and Greenland ice sheets. Science, 315, 1529-1532.

Shepherd, A., Wingham, D. J., Mansley ,J. A. D. & Corr, H. F. J. (2001). Inland thinning of Pine Island Glacier, West Antarctica. Science, 291, 862-864.

Shukla, A., Arora, M. K. & Gupta R. P. (2011). Synergistic approach for mapping debris-covered glaciers using optical-thermal remote sensing data with inputs from geomorphometric parameters. Remote Sensing of Environment, 114(7), 1378-1387.

Sidjak, R. W. & Wheate, R. D. (1999). Glacier mapping of the Illecillewaet icefield, British Columbia, Canada, using, Landsat TM and digital elevation data. International Journal of Remote Sensing, 20(2), 273-284.

Skvarca, P., Raup, B. & De Angelis, H. (2003). Recent behaviour of Glaciar Upsala, a fast-flowing calving glacier in Lago Argentino, southern Patagonia. Annals of Glaciology, 36, 184-188.

Smith, B. E., Fricker, H. A., Joughin, I. R. & Tulaczyk, S. (2009). An inventory of active subglacial lakes in Antarctica detected by ICESat (2003-2008). Journal of Glaciology, 55(192), 573-595

Sørensen, L. S., Simonsen, S. B., Nielsen, K., Lucas-Picher, P., Spada, G., Adalgeirsdottir, G., Forsberg, R. & Hvidberg, C. S. (2011). Mass balance of the Greenland ice sheet (2003–2008) from ICESat data – the impact of interpolation, sampling and firn density. The Cryosphere, 5(1), 173-186.

Soruco, A., Vincent, C., Francou, B., Ribstein, P., Berger, T., Sicart, J.E., Wagnon, P., Arnaud, Y., Favier, V., & Lejeune, Y. (2009). Mass balance of Glaciar Zongo, Bolivia, between 1956 and 2006, using glaciological, hydrological and geodetic methods. Annals of Glaciology, 50, 1-8.

Span, N. & Kuhn, M. (2003). Simulating annual glacier flow with a linear reservoir model. Journal of Geophysical Research-Atmospheres, 108(D10), 4313.

Strozzi T., Luckman, A., Murray, T., Wegmüller, U. & Werner, C. (2002). Glacier motion estimation using SAR offset-tracking procedures. IEEE Trans. Geosc. Remote Sens., 40(11), 2384-2391.

Ticconi, F., Shepherd, A., Muir, A., Mohold, G., Rinne, E. & Paul, F. (2012). Preliminary Results on Algorithm and Sensor Comparisons for the Estimation of Surface Elevation Changes over Ice Caps using Altimetry Data. 20 Years of Progress in Radar Altimetry Symposium, Venice, Italy.

VanLooy, J. A. & Forster, R. R. (2008). Glacial changes of five southwest British Columbia icefields, Canada, mid-1980s to 1999. Journal of Glaciology, 54(186), 469-478.

Van Niel, T. G., McVicar, T. R., Li, L. T., Gallant, J. C. & Yang, Q. K. (2008). The impact of misregistration on SRTM and DEM image differences. Remote Sensing of Environment, 112(5), 2430-2442.

Werner, C., Wegmüller, U., Strozzi, T. & Wiesmann, A. (2005). Precision estimation of local offsets between SAR SLCs and detected SAR images. Proceedings of IGARSS 2005, Seoul, Korea.

Williams, R. S., Jr., Hall, D. K. & Benson, C. S. (1991). Analysis of glacier facies using satellite techniques, Journal of Glaciology, 37, 120 - 127.

Williams, R. S., Jr., Hall, D. K., Sigurdsson, O. & Chien, J. Y. L (1997). Comparisson of satellite-derived with ground-based measurements of the fluctuations of the margins of Vatnajökull, Iceland, 1973-1992. Annals of Glaciology, 24, 72 -80.

Willis, M. J., Melkonian, A. K., Pritchard, M. E. & Ramage, J. M. (2012). Ice loss rates at the Northern Patagonian Icefield derived using a decade of satellite remote sensing. Remote Sensing of Environment, 117, 184-198.

Wingham, D. J., Ridout, A., Scharroo, R., Arthern, R. & Shum, C. K. (1998). Antarctic elevation change from 1992 to 1996. Science, 282, 456-458.

Wulder, M. A., Masek, J. G., Cohen, W. B., Loveland, T. R. & Woodcock, C. E. (2012). Opening the archive: How free data has enabled the science and monitoring promise of Landsat. Remote Sensing of Environment, 122, 2-10.

Zemp, M., Jansson, P., Holmlund, P., Gärtner-Roer, I., Koblet, T., Thee, P. & Haeberli, W. (2010). Reanalysis of multi-temporal aerial images of Storglaciären, Sweden (1959-1999); Part 2: Comparison of glaciological and volumetric mass balances. The Cryosphere, 4(3), 345-357.

Zwally, H. J., Brenner, A. C., Major, J. A., Bindschadler, R. A. & Marsh, J. G. (1989). Growth of Greenland Ice-Sheet - Measurement. Science, 246, 1587-1589.

Tables

Table 1: Overview table of automatically generated DEMs, with SRTM and ASTER being free of charge and with (quasi) global glacier coverage. Several other sources exist but may not offer off-the-shelf DEM products, having only local coverage and/or have purchasing charges. The TanDEM-X DEM has not yet beenreleased.

Data	Acquisition Type	Resolution	Time Period
SRTM	Radar interferometry	30-90 m	February, 2000
ASTER	Optical photogrammetry	30 m	2000-present
SPOT5-HRS (SPIRIT Products)	Optical photogrammetry	40 m	2002-present
TanDEM-X	Radar interferometry	12 m	2010-present

Table 2: Co-registration parameters from the three automatic algorithms tested: A is the robust surface matching, B is the brute-force iterative minimisation of difference residuals and C is the analytical solution using slope/aspect. The last row of the table shows the triangulation residuals between the three elevation datasets. Also shown are co-registration parameters and triangulation residuals between two DEMs and the collection of ICESat altimetry available over the scenes.

DEM differences / Triangulation*	Method	ΔX	ΔY	ΔZ
2000 - 2006	A	24.4	21.8	7.6
	B	-5.6	-50.8	2.5
	C	24.3	20.6	3.2
2000 - 2002	A	-12.0	-4.6	-1.0
	B	-41.1	-24.5	-4.6
	C	-13.4	-9.1	-4.1
2002 - 2006	A	-36.3	-25.8	-8.5
	B	-38.0	25.4	-4.9
	C	-38.4	-26.2	-7.5
2000 - ICESat	A	11.6	-14.4	-8.5
	B	-	-	-
	C	-1.71	-3.90	-3.80
2006 - ICESat	A	25.3	18.4	9.9
	B	-	-	-
	C	25.78	12.68	-0.25
2000 - 2002 - 2006*	A	0.1	0.6	0.1
	B	-2.5	-0.8	2.2
	C	-0.6	3.5	-0.2
2000 - 2006 - ICESat*	A	10.7	-11.0	-10.8
	B	-	-	-
	C	-3.09	3.99	-0.35

Table 3: Overview of the algorithms applied to each test site: dataset used and relative temporal coverage.

Algorithm	Devon Ice Cap		Austfonna	
	Sensor	***Temporal coverage***	***Sensor***	***Temporal coverage***
DS-RT-RepAlt	ICESat/GLAS	2003-2009		
DP-RT-RepAlt			ICESat/GLAS	2003-2009
RP-RT-RepAlt	ICESat/GLAS	2003-2009	ICESat/GLAS	2003-2009
XO-RepAlt			Envisat/RA-2	2002-2010

Table 4: Average and standard deviation values of the dh/dt obtained within elevation intervals of 100 m for the DP-RT-RepAlt, the RP-RT-RepAlt, the XO-RepAlt algorithms applied to ICESat data (2003-09) and for the repeated airborne laser profiles (1996-2002); the last three columns reportthe absolute differences between the average values of the DP-RT-RepAlt, the RP-RT-RepAlt and the XO-RepAlt algorithms applied and the average values of the airborne dataset, respectively.

h (m)	**dh/dt (m/yr) DP-RT-RepAlt (1)**	**dh/dt (m/yr) RP-RT-RepAlt (2)**	**dh/dt (m/yr) XO-RepAlt (3)**	**dh/dt (m/yr) airborne**	**|Δ| (m/yr) (1)**	**|Δ| (m/yr) (2)**	**|Δ| (m/yr) (3)**
0 - 100	----	----	----	----	----	----	----
100 - 200	-0.81±0.95	-0.87±0.76	0.58±0.94	-0.21±0.19	0.60	0.66	0.79
200 - 300	-0.10±0.70	-0.19±0.60	0.59±0.52	-0.13±0.16	0.03	0.06	0.46
300 - 400	0.27±0.72	0.29±0.53	0.09±0.13	-0.28±0.15	0.55	0.57	0.37
400 - 500	0.43±0.91	0.33±0.53	0.31±0.12	0.07±0.27	0.35	0.25	0.23
500 - 600	0.48±0.55	0.50±0.45	-0.21±1.45	0.20±0.26	0.28	0.30	0.41
600 - 700	0.53±0.57	0.64±0.37	0.43±0.12	0.34±0.19	0.19	0.30	0.09
700 - 800	0.76±0.77	0.74±0.51	0.28±0.24	0.34±0.18	0.43	0.40	0.05

Table 5: Summaries of the RMSE (m/yr) and the correlation coefficient R obtained from the validation activity.

RMSE (m/yr)/R	DS-RT-RepAlt (laser alt.)	DP-RT-RepAlt (laser alt.)	RP-RT-RepAlt (laser alt.)	XO-RepAlt (radar alt.)	airborne
DS-RT-RepAlt (laser alt.)	---	N/A	0.47/0.48	N/A	N/A
DP-RT-RepAlt (laser alt.)	---	---	0.41/0.89	1.65/0.01	0.39/0.73
RP-RT-RepAlt (laser alt.)	---	---	---	1.25/-0.02	0.41/0.74
XO-RepAlt (radar alt.)	---	---	---	---	0.47/-0.23
airborne	---	---	---	---	---

Table 6: Performances of the algorithms applied: for repeat-track methods the spatial density is intended as the ratio between the number of grid cells with valid elevation change measurements and the total number of grid cells covering the areas if interest, whereas for the cross-over method the spatial density is given by the ratio between the number of dh/dt values and the total number of satellite orbit cross-over points (in percentage).

	Algorithms applied over Devon Ice Cap			Algorithms applied over Austfonna Ice Cap		
	DS-RT-RepAlt	RP-RT-RepAlt	XO-RepAlt	DP-RT-RepAlt	RP-RT-RepAlt	XO-RepAlt
Spatial density	4%	5%	< 1%	5%	5%	2%
Spatial coverage	75%	75%	< 5%	75%	75%	60%
Temporal density	1.6 $year^{-1}$	1.6 $year^{-1}$	10 $year^{-1}$	1.6 $year^{-1}$	1.6 $year^{-1}$	10 $year^{-1}$
CPU	< 1 h	< 1 h	1 day	1 h	1 h	1 day
Manpower time	0.5 day	0.5 day	1 week	0.5 day	0.5 day	1 week
Accuracy	0.40 m/yr	0.40 m/yr	0.50 m/yr	1 m/yr	0.3 m/yr	0.5 m/yr

Table 7: Summary of the ice cap elevation change algorithm performance in relation to the selection criteria (Good=3 scores, Moderate=2 scores, Poor=1 score).

	DS-RT-RepAlt	DP-RT-RepAlt	RP-RT-RepAlt	XO-RepAlt
RMSE	Good	Good	Good	Poor
Spatial density	Good	Good	Good	Poor
Temporal density	Moderate	Moderate	Moderate	Good
Processing time	Good	Good	Good	Moderate
TOTAL SCORE	11	11	11	7

Figure captions

Fig. 1: Global map showing the approximate location of the test regions described in this study. Geographic coordinates are: Fig. 2: 46.53 N, 8.2 E; Fig. 3: 42.25 S, 72.15 W; Fig. 4: 34.15 N, 75.75 E; Fig. 5: 43.65 S, 170.25 W; Fig. 9: 79.8 N, 22.1 E; Fig. 10: 35.9 N, 75.9 E (left) and 35.75 N, 76.4 E (right); Fig. 11: 64.2 N, 16.4 W.

Figure 2: The impact of the threshold value for the band ratio and the median filter is shown for a test region in the Swiss Alps with Oberaar glacier (OA) in the centre. a) Three glacier maps combined resulting from three threshold values: 1.8 (all colours), 1.9: (grey and blue), 2.0 (grey). b) Effect of a 3 × 3 median filter: red pixels are removed and blue pixels are added (shown here for the map with the threshold 1.9).

Figure 3: Glacier outlines for the test region in Chile / Argentina with five different values of the threshold in band TM1 applied (blue: 100, green: 90, white: 80, red: 70, yellow: 60). Substantial changes take only place in regions with ice and snow located in cast shadow. The finally selected threshold value in TM1 is 65.

Figure 4: Overlay of the glacier outlines from the different participants for the subset of the test region located in the Himalaya where editing of wrong classification results was requested.

Figure 5: For a test region in New Zealand the DEM differencing was investigated. (a) hillshade of the SRTM DEM; (b) elevation differences between the SRTM and 2006 ASTER DEM plotted in grayscale pre co-registration thus displaying the "false-hillshade"; (c) the elevation differences after co-registration; (d) histograms of the elevation differences before and after- co-registration; (e) plot of the slope normalized elevation differences by aspect pre co-registration and the solutions to equation (1) after the first (blue) and second iterations (red); and (f) shows the same as e) but post co-registration.

Figure 6: Scatter-plot of the *dh/dt* results obtained using: a) the RP-RT-RepAlt and the DS-RT-RepAlt algorithms over Devon Ice Cap; b) the DP-RT-RepAlt and the RP-RT-RepAlt algorithms over Austfonna.

Figure 7: Absolute differences in m/yr as function of the elevation between airborne dh/dt and DP-RT-RepAlt dh/dt (blu); airborne dh/dt and RP-RT-RepAlt *dh/dt* (red); airborne dh/dt and XO-RepAlt dh/dt (green) for the Ausfonna Ice Cap (Svalbard).

Figure 8: a) Scatter-plot of the dh/dt results obtained using the DP-RT-RepAlt and the XO-RepAlt algorithms; b) scatter-plot of the dh/dt results obtained using the RP-RT-RepAlt and the XO-RepAlt algorithms.

Figure 9: From left to right: slant-range interferogram, slant-range and azimuth displacement maps from offset-tracking, and multiple-aperture interferogram (Gourmelen et al., 2011) based on a ALOS PALSAR image pair separated by 46 days over Vestfonna (Svalbard). Only offset-tracking is able to derive information over the outlet glaciers, the interferograms are decorrelated.

Figure 10 : Velocity fields derived from satellite optical data over Biafo (left column) and Baltoro glaciers (right column), Karakoram. From top to bottom: First row: Method (4) of section 5.3 unfiltered, second row: Method (4) filtered with correlation coefficient threshold and smoothing, third row: Method (3) unfiltered, forth row: Method (1) weakly filtered, fifth row: Method (2) of section 5.3 filtered.

Figure 11: Displacement magnitude in slant range geometry over Breidamerkurjökull (Iceland) from each of the round-robin participants using the cross-correlation of image chips in a TerraSAR-X amplitude image pair separated by 11 days. The following matching window sizes and oversampling factors were considered (range x aximuth/ oversampling): Dataset 1: 128 x 128 / 2, Dataset 2: 128 x 128 / 16, Dataset 3: 128 x 128 / 2, Dataset 4: 64 x 64 / 16, Dataset 5: 44 x 40 / 4. Despite similar matching parameters (e.g. Datasets 1 and 3), different correlation thresholds chosen by the participants produced variable results.

Figure 12: Polar plot of ground-range and azimuth displacements over stable ground based on two results (depicted in red and green) from the round-robin over Vestfonna (Svalbard) using a ALOS PALSAR image pair separated by 46 days (for 20248 points). Standard deviations are on the order of 0.5 m, corresponding to total horizontal displacement rates of about 6 m/yr.

Figure 13: Comparison of SAR and DGPS horizontal ice speeds over Vestfonna (Svalbard) using a ALOS PALSAR image pair separated by 46 days for two participants of the round robin. DGPS data are from geodetic survey campaigns in 2007-2010 considering 13 stations (Pohjola et al., 2011). The averages of the absolute difference between DPGS and SAR results are 9.6 m/yr and 7.6 m/yr in the two cases.

Figures

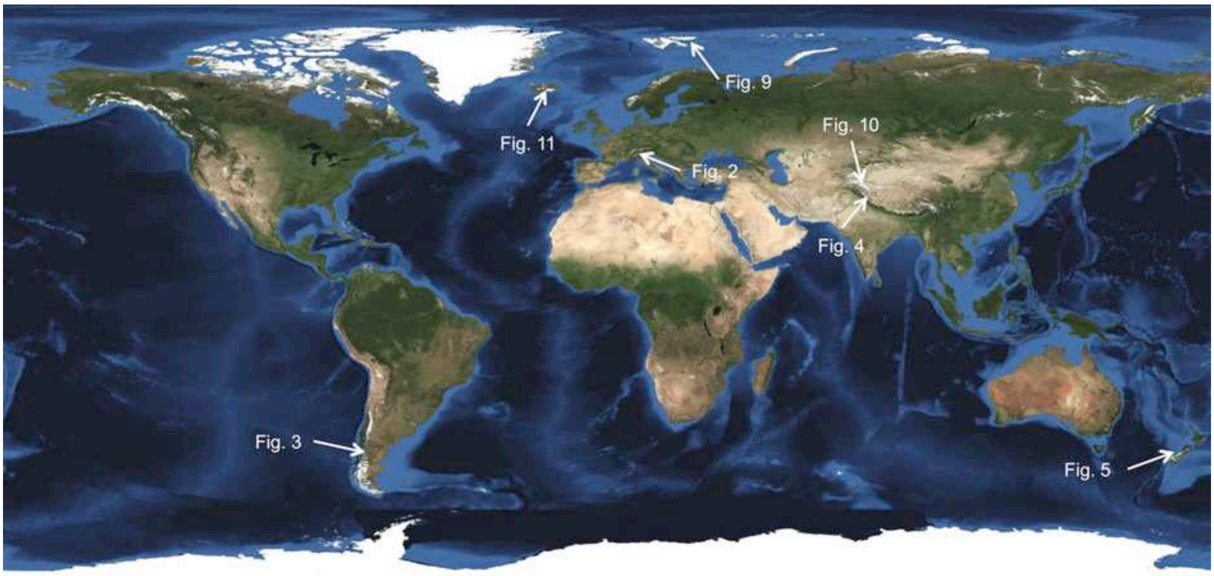

Fig. 1

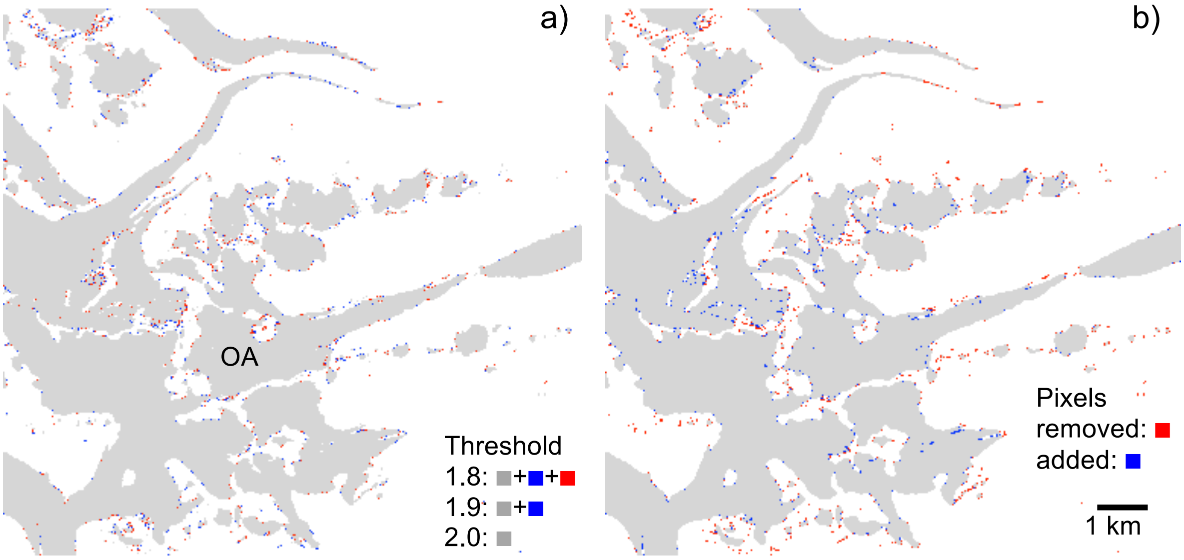

Fig. 2

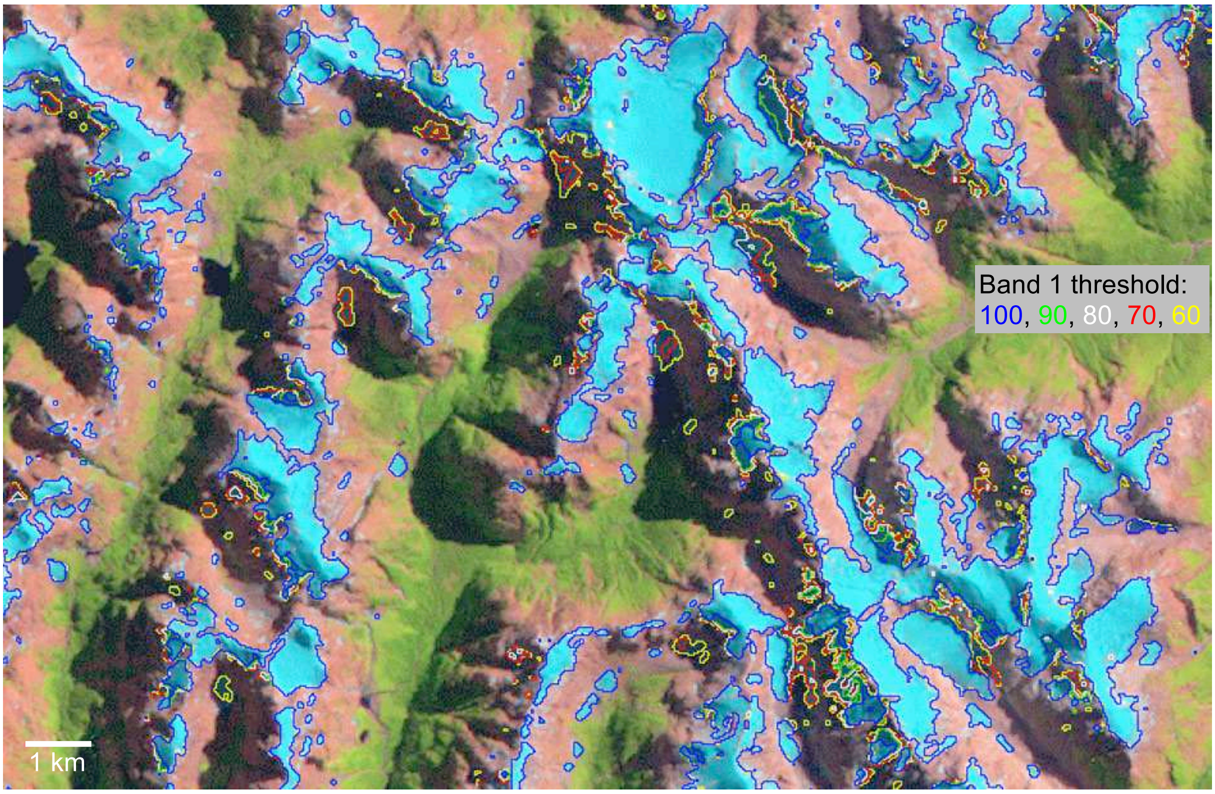

Fig. 3

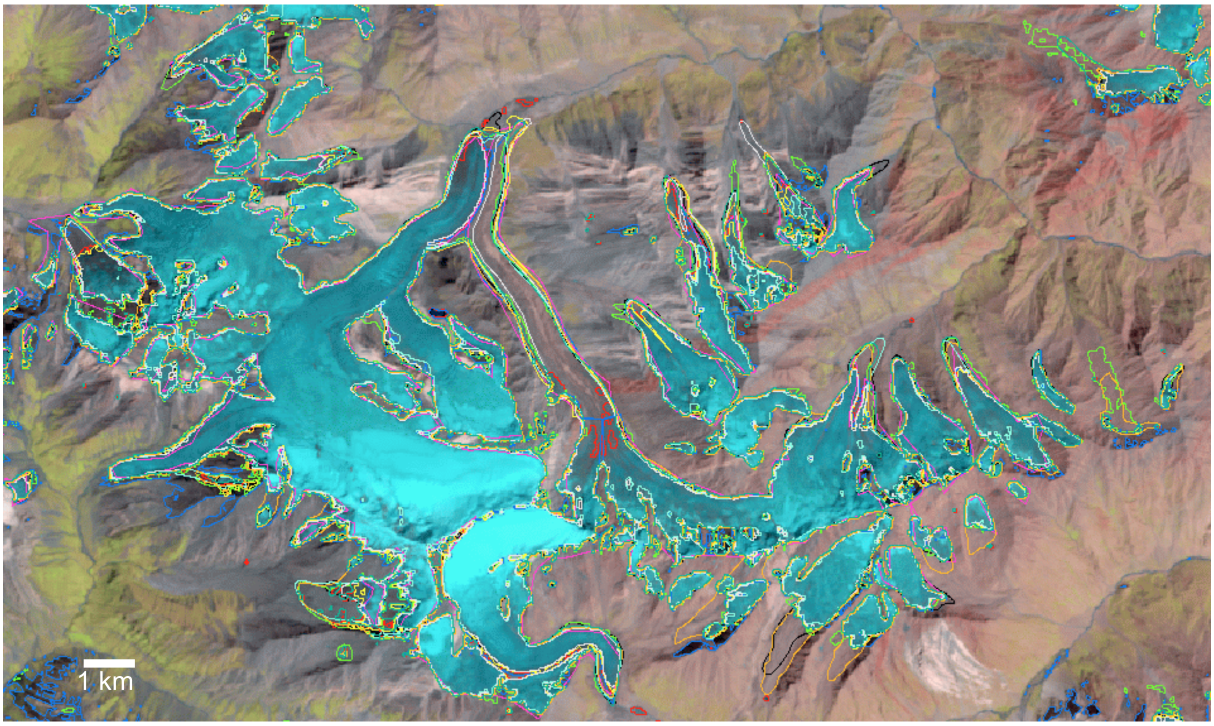

Fig. 4

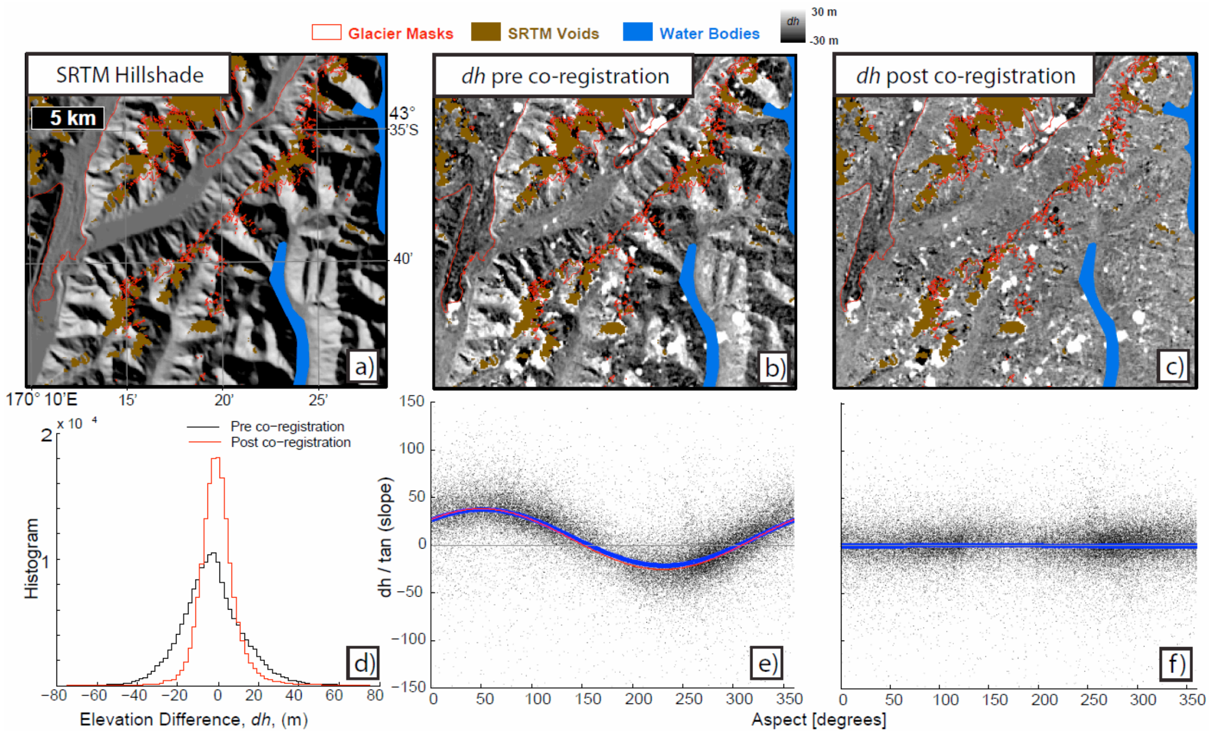

Fig. 5

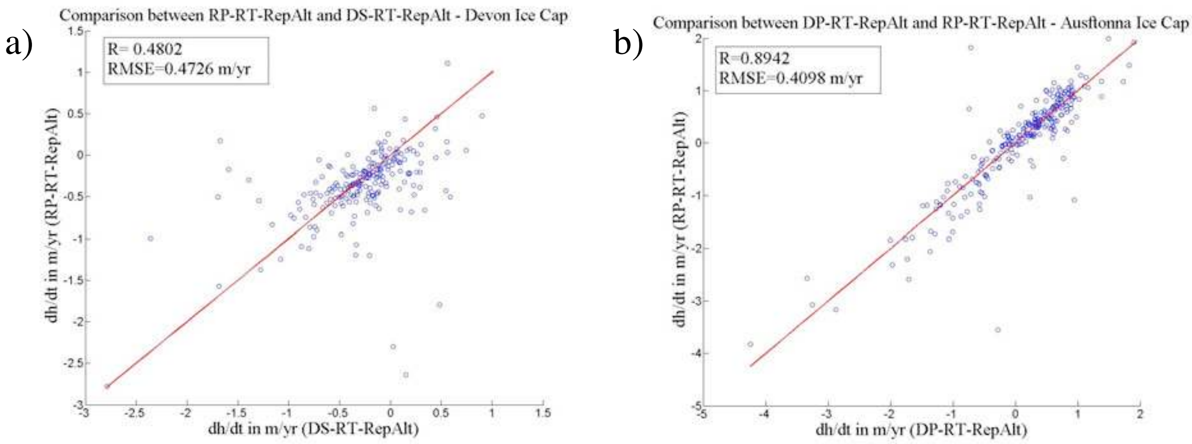

Fig. 6

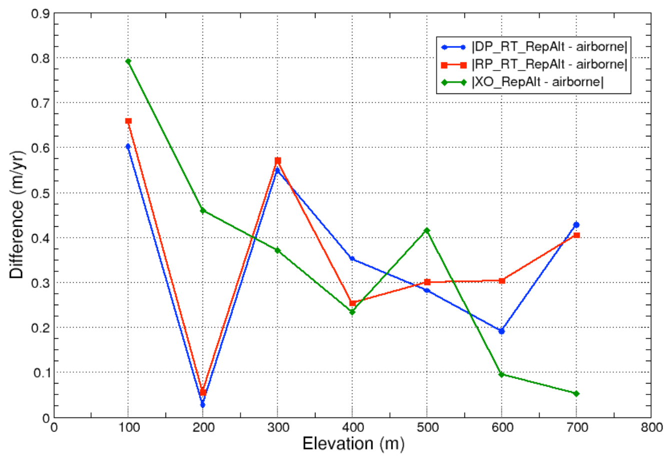

Fig. 7

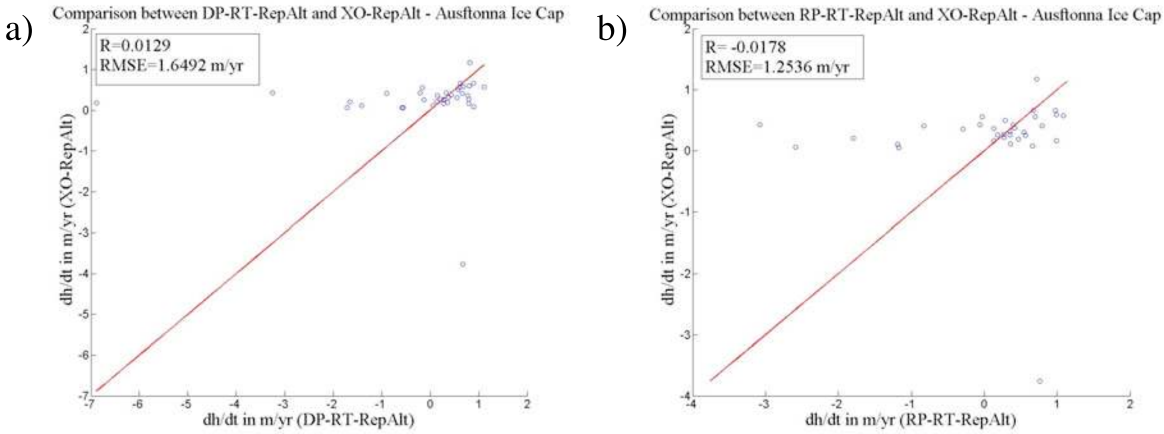
a)
Comparison between DP-RT-RepAlt and XO-RepAlt - Ausftonna Ice Cap
R=0.0129
RMSE=1.6492 m/yr
dh/dt in m/yr (XO-RepAlt)
dh/dt in m/yr (DP-RT-RepAlt)
b)
Comparison between RP-RT-RepAlt and XO-RepAlt - Ausftonna Ice Cap
R= -0.0178
RMSE=1.2536 m/yr
dh/dt in m/yr (XO-RepAlt)
dh/dt in m/yr (RP-RT-RepAlt)

Fig. 8

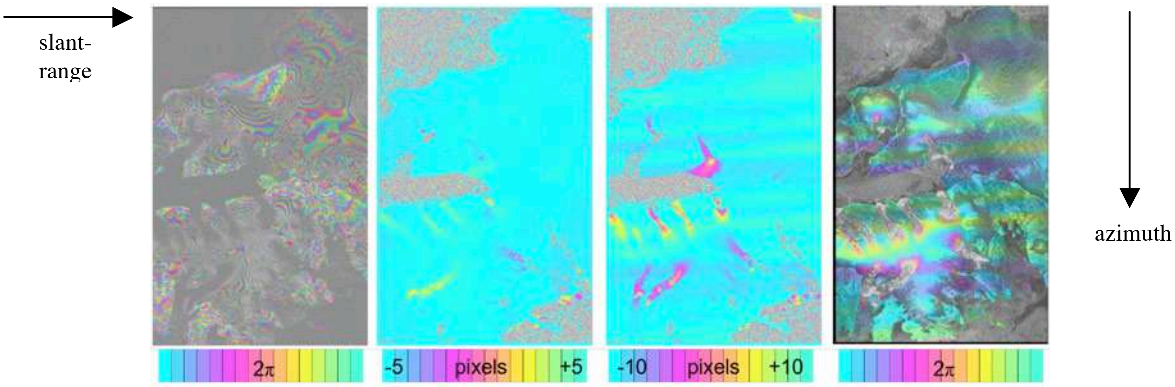
slant-
range
azimuth
2π
-5 pixels +5
-10 pixels +10
2π

Fig. 9

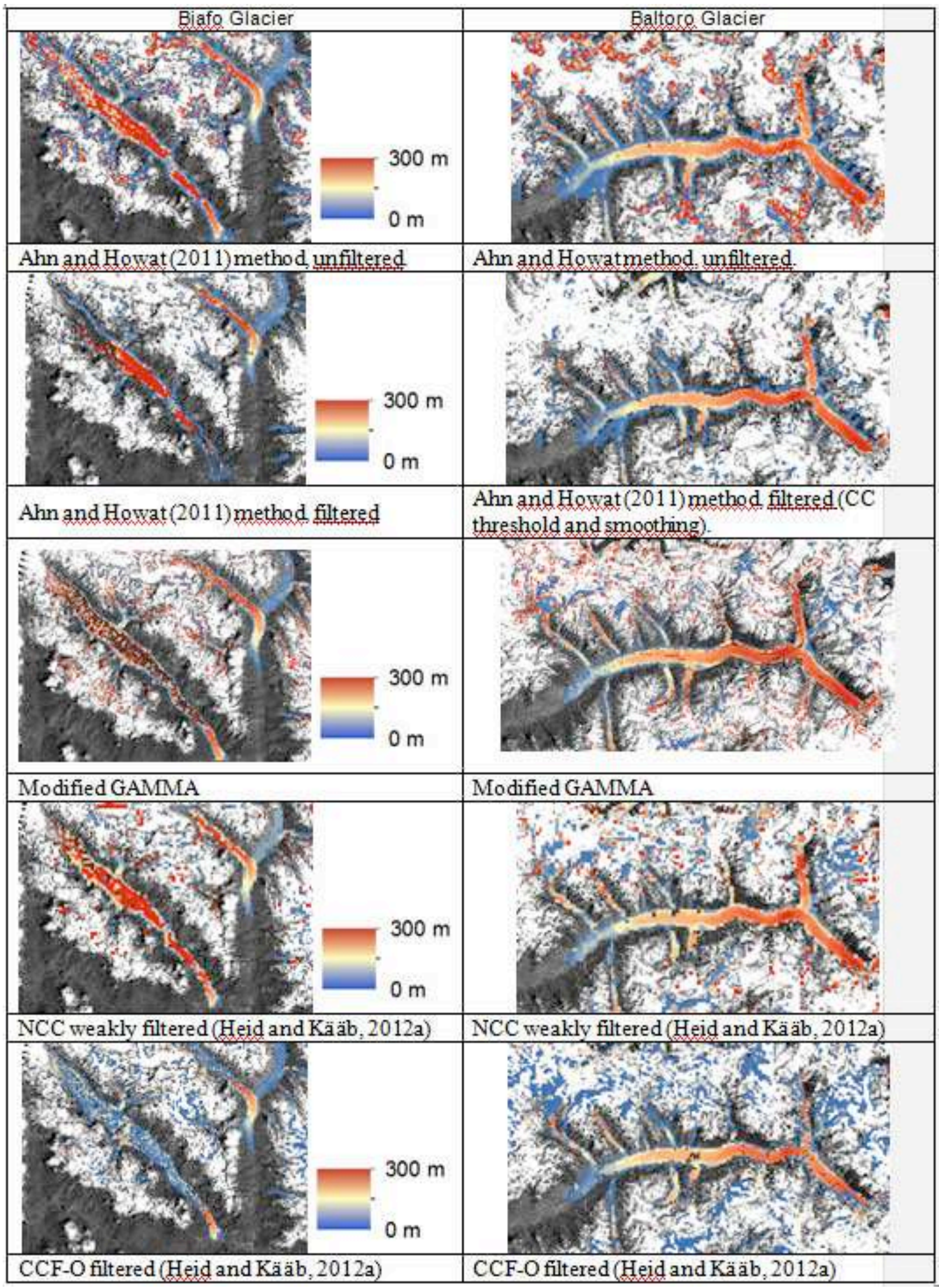
Biafo Glacier
Baltoro Glacier
300 m
0 m
Ahn and Howat (2011) method, unfiltered
Ahn and Howat method, unfiltered.
Ahn and Howat (2011) method, filtered
Ahn and Howat (2011) method, filtered (CC threshold and smoothing).
Modified GAMMA
Modified GAMMA
NCC weakly filtered (Heid and Kääb, 2012a)
NCC weakly filtered (Heid and Kääb, 2012a)
CCF-O filtered (Heid and Kääb, 2012a)
CCF-O filtered (Heid and Kääb, 2012a)

Fig. 10

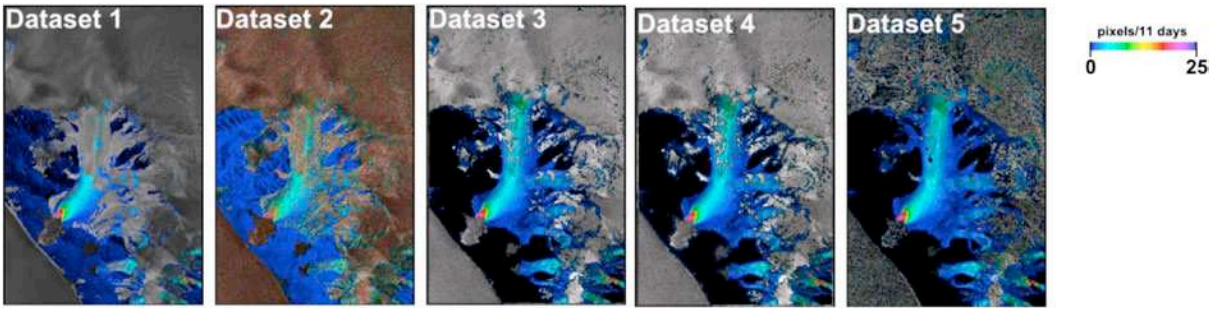

Fig. 11

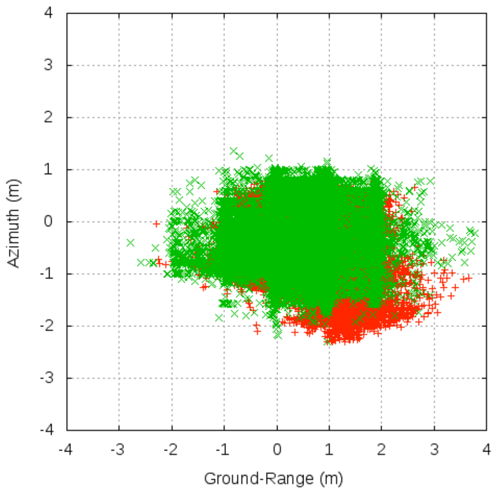

Fig. 12

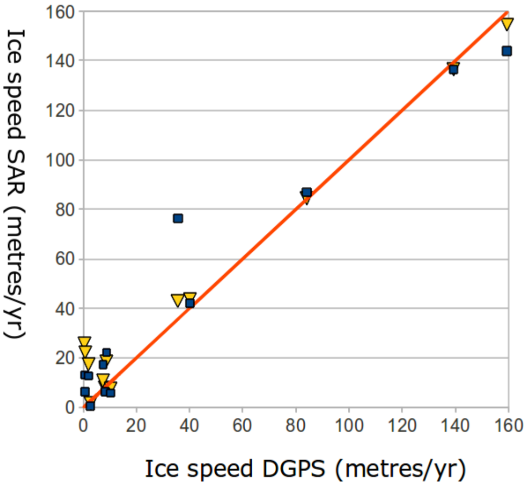

Fig. 13

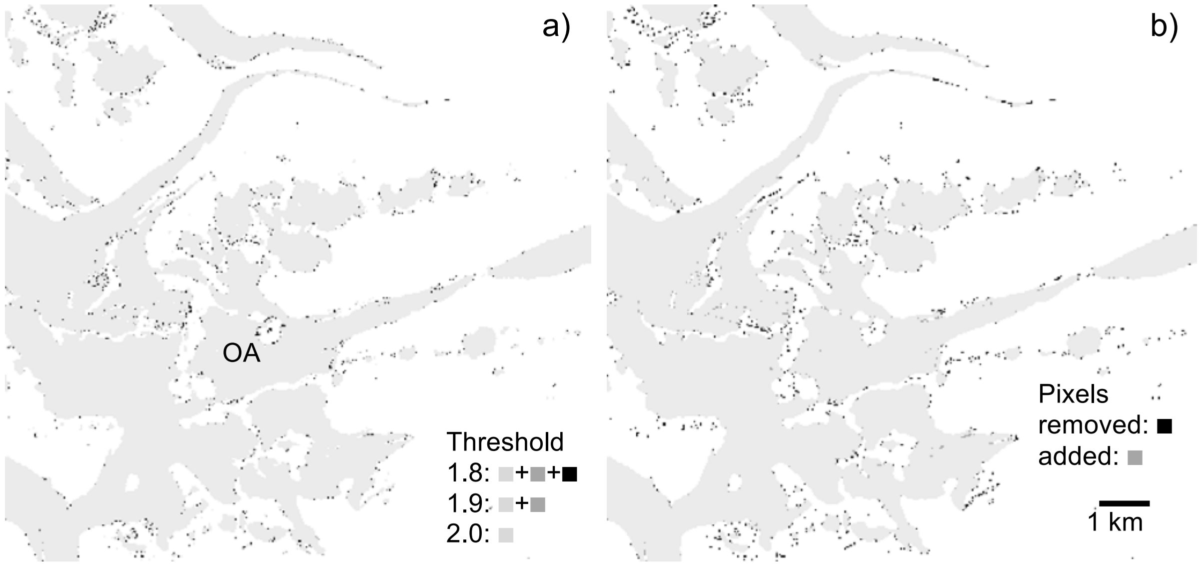

Fig. 2